energies

MDPI

Article

The Interplay Between Combustion and Component Thermal Loading in Next-Generation Marine Engines Employing Reactivity-Controlled Compression Ignition

Alireza Kakoee [1,*], Kian Golbaghi [1], Alberto Cafari [2], Aneesh Vasudev [1], Sadegh Mehranfar [3], Amin Mahmoudzadeh Andwari [3], Ben Smulter [2], Jari Hyvönen [2] and Maciej Mikulski [1,*]

[1] Efficient Powertrain Solutions (EPS), School of Technology and Innovation, University of Vaasa, Yliopistonranta 10, P.O. Box 700, 65200 Vaasa, Finland; kian.golbaghi@uwasa.fi (K.G.)
[2] Engine Research and Technology Development at Wärtsila Marine Solutions, P.O. Box 1434, 65200 Vaasa, Finland
[3] Machine and Vehicle Design (MVD), Materials and Mechanical Engineering, Faculty of Technology, University of Oulu, P.O. Box 8000, 90014 Oulu, Finland; amin.andwari@oulu.fi (A.M.A.)
* Correspondence: alireza.kakoee@uwasa.fi (A.K.); maciej.mikulski@uwasa.fi (M.M.)

Abstract

Energy transition demands cleaner and more efficient marine engines, accelerating the development of reactivity-controlled compression ignition (RCCI) concepts with multi-fuel capability. However, the coupling between combustion behavior and thermal loading in RCCI engines remains insufficiently understood due to limited experimental capabilities and the absence of integrated modeling tools. This study develops a rapid predictive framework that dynamically couples an in-house chemical-kinetics solver with a GT-Suite engine model and a finite-element wall thermal solver. The framework was calibrated against measurements from a single-cylinder research engine representative of the Wärtsilä 31DF medium-speed NG/LFO RCCI engine. It accurately captured component temperatures and combustion/performance parameters with RMS errors below 5% and cycle times under four minutes. The results show that RCCI operation introduces pronounced component temperature variations across the load range, creating challenges for thermal management and combustion control. Low-load combustion inefficiencies were linked to cylinder head thermal design rather than the conventional flame-quenching explanation. At high load, excessive pressure-rise rates amplified heat transfer demands, with exhaust-valve temperatures exceeding 780 K and posing pre-ignition risks. Increasing coolant temperature by 40 K reduced methane slip by 10% and advanced combustion by nearly 2 CAD, improving efficiency at low load, while coordinated lambda/fuel-blend control lowered peak combustion temperature by ~200 K at high load, mitigating thermal-induced pre-ignition without compromising performance or emissions.

Keywords: combustion; emission; thermal management; RCCI; low temperature combustion; 1D modeling; multi-zone model; MZM; UVATZ

Academic Editors: Zongyu Yue, Haifeng Liu and Chao Jin

Received: 17 November 2025
Revised: 8 December 2025
Accepted: 17 December 2025
Published: 23 December 2025

1. Introduction

Reactivity-controlled compression ignition (RCCI), achieved through in-cylinder blending of low-reactivity fuels (LRFs) and high-reactivity fuels (HRFs), has gained significant attention as a promising low-emission, high-efficiency combustion concept for large-bore engines [1–3]. RCCI offers improved combustion controllability and fuel flexibility

https://doi.org/10.3390/en19010083

compared with homogeneous charge compression ignition (HCCI) [4], and its reactivity-stratified heat release has been shown to enable high thermal efficiency with inherently low NO_x and soot emissions [5,6]. The authors' research group has contributed to the development of RCCI concepts for next-generation marine engines in collaboration with Wärtsilä Energy Solutions [7,8], culminating in successful sea trials onboard the M/V Aurora Botnia. These trials demonstrated an order-of-magnitude NO_x reduction and nearly 50% lower methane slip relative to best-in-class dual-fuel engines [9].

Despite these advantages, RCCI faces practical limitations, including low-load hydrocarbon emissions [10], combustion stability concerns [11], high pressure rise rate (PRR) [12], and sensitivity to reactivity and thermal stratification [13]. Gas temperature strongly influences auto-ignition chemistry, and cold boundary layers are known to slow or suppress reactions, particularly at low loads [14,15]. Several studies have highlighted the influence of wall temperatures on combustion characteristics and emissions in marine engines [16], and transient wall conduction models have shown substantial cyclic variations that directly affect RCCI control [11,17]. These findings position thermal and compositional stratification immediately behind chemical kinetics as key challenges in predictive RCCI modeling.

Model-based development is increasingly relied upon to navigate the high calibration effort of RCCI systems. Physics-based multi-zone models (MZMs) offer a balance between detailed CFD and empirical approaches, achieving predictive accuracy with orders-of-magnitude shorter runtimes than CFD [2,3,18]. However, no universal MZM toolchain exists, and commercial low-temperature combustion (LTC) solutions remain limited [17,19,20]. Recent work by Vasudev et al. [17] produced a comprehensive RCCI MZM with fuel stratification, wall heat loss, turbulence-based mixing, and zonal configuration. RCCI modeling is further complicated by inherently transient airpath dynamics involving the intake manifold, turbocharger, intercooler, and exhaust system. These interactions critically influence airflow, pressure, and combustion phasing, making their accurate representation essential for system-level fidelity. For these reasons, 1D engine simulation frameworks—especially GT-Power—have become widely adopted due to their flexibility, predictive capabilities, and favorable computational cost [21,22].

Various researchers have employed 1D–3D hybrid approaches to explore dual-fuel and LTC combustion. Stoumpos et al. [22] evaluated nitrogen oxide reduction in lean-burn dual-fuel operation, while Sixel et al. [23] used a GT-Power-integrated combustion model to study methanol dual-fuel combustion. TNO's multi-zone model [24] and its application to natural-gas stratification [14] further demonstrated the importance of reactivity and thermal stratification in RCCI. These studies also identified challenges such as knocking, incomplete combustion, and the formation of fuel-rich zones in reactivity-stratified mixtures, contributing to NO_x, soot, CO, and UHC emissions [17]. The strong temperature gradients near the combustion chamber walls—formed within a thin boundary layer—were shown to have a decisive influence on flame quenching and emissions formation [25–34].

The sensitivity of RCCI to wall temperatures has motivated detailed investigations into thermal boundary conditions across diesel and dual-fuel engines [16,24,28–32]. This motivates the use of computational models to supplement limited experimental accessibility. Accurate prediction of spatial and temporal wall temperatures is essential for understanding combustion efficiency, heat losses, emissions, and component durability [35–40].

Heat transfer between gas and chamber walls may be modeled using empirical correlations such as those proposed by Annand [41], Hohenberg [42], and Woschni [43], though these often overpredict heat losses in LTC conditions [44–46]. More advanced approaches include turbulence-enhanced correlations, boundary-layer modeling, and methods targeting wall temperature prediction directly [14,47–50]. Coupled 1D thermal networks and lumped-mass models have been widely adopted for system-level thermal analysis [23,24,51–54]. While

CFD–CHT simulations provide detailed thermo-structural interaction [55–60], they remain computationally expensive for design loops. Enhanced 1D–3D hybrid frameworks, incorporating finite element meshes, have demonstrated improved accuracy in heat rejection prediction and component temperature estimation while retaining computational efficiency [61–63].

Recent progress includes the coupling of the UVATZ physics-based chemical-kinetics multi-zone model with GT-Power by Kakoee et al. [26], enabling predictive RCCI–airpath simulations calibrated on a single-cylinder research engine representative of the Wärtsilä 31DF platform. Their results showed good agreement with in-cylinder pressures and performance metrics, with deviations within 2%. Since RCCI remains highly sensitive to thermal boundary conditions, improving the integration of combustion models with detailed component temperature prediction has become a critical step toward fully predictive system-level RCCI simulation.

Motivation, Goal, and Objectives of the Present Study

In light of the above review, it was recognized that understanding the relationship between combustion and thermal effects is crucial for improving the efficiency of RCCI engines and enhancing emission control. The phenomena remained incompletely understood, hindered by the limited maturity of experimental setups and the use of decoupled simulation toolchains. In particular, within the context of emission performance calibration, managing the phenomenological complexity of thermal effects in RCCI within an extremely large control parameter space required fast in-cylinder models that simultaneously resolved combustion and made predictive estimation of component temperatures.

The marine industry was identified as the bridge for introducing RCCI technology to next-generation dual-fuel engines. The high technology readiness level (TRL) substantiated the infrastructural efforts necessary to bridge this knowledge gap. To this end, the present work developed a rapid simulation framework capable of predicting the interplay between RCCI combustion and thermal effects associated with various cylinder components, under the constraint of quasi-dimensional in-cylinder flow. An in-house chemical-kinetics-based solver integrated into the GT-Suite engine model (Kakoee et al. [20]) was dynamically coupled with a finite element method (FEM)-based wall thermal solver. The models were first calibrated independently, using comprehensive data from a single-cylinder research engine that represented the geometry of the state-of-the-art Wärtsilä 31DF engine. To this end, experiments were performed to comprehensively characterize RCCI combustion and the gas-side temperatures of individual cylinder components under fully controllable boundary conditions.

The coupled models were then thoroughly validated, and the developed framework was applied to address key knowledge gaps related to thermal mechanisms in RCCI combustion and their impact on thermal loading of components. The study defined six overarching research objectives designed to bridge the gap between fundamental combustion science and the major challenges affecting the applicability of RCCI in next-generation fuel-flexible marine engines:

O1. Validate the new framework using comprehensive experimental data;

O2. Benchmark component thermal loading at different RCCI operating conditions;

O3a. Determine the sensitivity of RCCI combustion to wall temperature, considering spatially diversified heat transfer paths;

O3b. Examine the feasibility of coolant and oil circuit temperature control for reducing methane slip at low engine loads;

O4a. Determine the sensitivity of wall temperature to RCCI operating conditions;

O4b. Examine the feasibility of coordinated airpath-combustion control for reducing thermal stress at high-load RCCI operation.

https://doi.org/10.3390/en19010083

The numbering of the objectives relates to the specific design of the experiments. The corresponding campaigns, 1–4, are described in detail toward the end of the methods outline.

2. Methodology

Experimental Setup and Reference Experimental Data

The RCCI validation data used in this study originated from the Wärtsilä Mono single-cylinder research engine (SCRE), which replicated the cylinder geometry of Wärtsilä's 310 mm bore dual-fuel engines. Table 1 presents the key specifications of the test rig, including the optimization of a centrally positioned twin-needle injector that was integrated into a high-pressure common-rail fuel system. This injector was optimized for the use of light fuel oil (LFO) as the HRF [64].

Table 1. Wärtsilä W31 single-cylinder research engine setup specifications.

Specification	**Description**
Displacement and nominal speed	32.45 L/720 rpm
Stroke/bore	1.39:1
Air system	External air compressor with air temperature and pressure control (up to 10 bar)
High-reactivity fuel system	Common-rail 2.0 with twin needle injector and multi-injection capability
Low-reactivity fuel system	Low-pressure, multi-point, upstream of the intake valves
Valvetrain	Four valve ports; variable intake valve closure (VIC); fixed exhaust valve opening (EVO)
Emission system	Horiba Mexa-One (NO_x, CO, THC, CO_2, O_2) AVL415S (FSN-soot)
Indicative system	AVL Indicom, cylinder pressure transducer Kistler 6124 A, 300 bar range, 30 pC/bar sensitivity.
Engine control	Rapid prototyping platform
Test fuels	ISO 8217 [65] compliant LFO/LNG (MN = 80)

In RCCI operation, the smaller needle was employed to improve atomization of micro-injected fuel quantities. Its narrow-cone tip supported reactivity stratification when operated with early injection timings. Natural gas, acting as the LRF, was supplied via a multi-point gas injector located upstream of the intake valve. During dual-fuel operation, the smaller needle was responsible for accurate delivery of pilot fuel, while the larger needle was used exclusively in conventional diesel mode. The SCRE was also equipped with a partially variable intake and exhaust valvetrain.

Unlike multi-cylinder engines, the SCRE lacked a turbocharger, which necessitated a tailored solution to regulate charge air pressure and temperature. The air system included two compressors, two buffer tanks, a charge air dryer, and two pressure-regulating valves, ensuring stable airflow and replication of real engine boundary conditions.

Table 1 also includes the measurement system used in the experiments. High-frequency, in-cylinder pressure was measured over 300 consecutive cycles with a 0.20 crank angle degree (CAD) resolution, along with pressure data from upstream and downstream of the cylinder head. These signals were post-processed to derive key performance indicators such as indicated mean effective pressure (IMEP) and crank angle at X% mass burned (CAX). Low-frequency measurements included fuel consumption, which was recorded using a Coriolis flow meter for gaseous fuels and a gravimetric balance for liquid, as well as intake air consumption.

Thermal boundary validation was supported by detailed temperature measurements of the intake and exhaust ports, and combustion chamber surfaces such as the piston top, liner, valves, and cylinder head. Pentronic K-type thermocouples were used for all component surface temperature measurements. The same thermocouple type, depth, and installation method were applied to the liner, flame plate (cylinder head), and piston top. The large piston size required multiple thermocouples: eight sensors on the cylinder head (flame plate); four sensors on the liner (two on the exhaust side, two on the intake side); sixteen sensors on various piston locations; and three sensors per valve for both intake and exhaust valves.

The data from piston-mounted sensors were transmitted via a battery-powered telemetry system. Measurements were captured at a 10 Hz frequency during operating cycles. Figure 1 illustrates the sensor layout across engine components, with colored circles highlighting the positions selected for comparison studies.

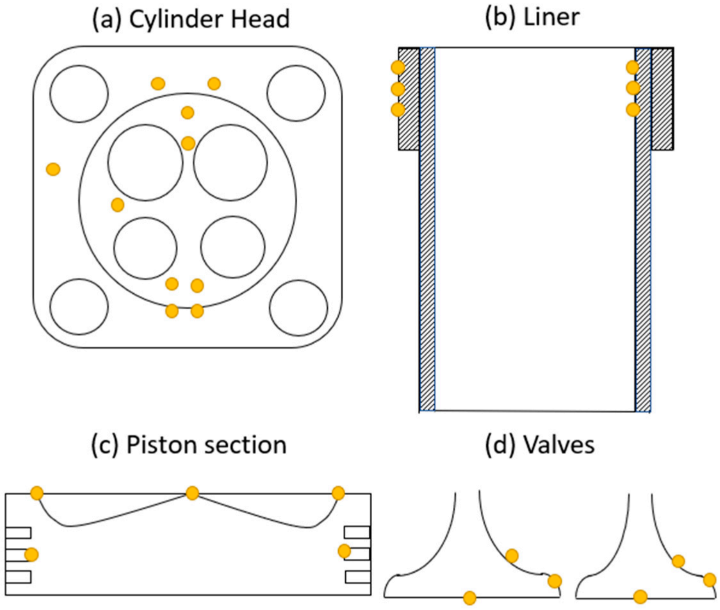

Figure 1. Temperature sensor location on various engine parts.

Measurements were performed at six distinct RCCI operating points. Table 2 lists the specifications of the reference experimental cases while highlighting the extent to which the present simulation study relied on the experimental data. The case specifications were expressed as relative values (ref) against a standard International Maritime Organization (IMO) Tier III low-load calibration point for the commercial variant of the Wärtsilä 31DF [66]. These specifications included, among others, the total air–fuel equivalence ratio (λ) and the energy-based blend rate (BR) of natural gas (NG) vs. light fuel oil (LFO).

Table 2. RCCI operating points from the Wärtsilä 31 SCRE used for model calibration and validation. The parameters characterizing the operating points are given as relative values with respect to "ref", which is a standard IMO TIER III low-load calibration point on the commercial variant of the engine, Wärtsilä 31DF, a multi-cylinder layout operating on the lean burn principle of NG-diesel. The final column indicates the extent to which the present study relied on the mentioned data [26].

Load Regime	Case	λ (–)	ΔBR from Ref [pp]	SOE [CA bTDC]	ΔTint [K]	Pint [bar]	Experimental Role
Low-load	A	ref + 1.8	−41.9	+65	0	+0.5	Validation
Part-load	B	ref + 1.0	−10.9	+65	0	+1.3	Calibration/Validation
Mid-load	C	ref + 0.5	+1.9	+50	−5	+3.7	Calibration
Mid-load	D	ref + 0.8	+2.4	+65	−5	+3.5	Validation
Mid-load	E	ref + 0.8	+0.9	+26	−5	+3.8	Validation
High-load	F	ref + 0.1	+0.9	+50	−7	+6.3	Investigation

The start of energizing of the LFO injector is labeled SOE, while the cycle-averaged intake manifold temperature and pressure are denoted as Tint and Pint, respectively. All measurements were conducted at a constant engine speed of 720 rpm.

3. Simulation Methods

3.1. Predictive Combustion Model

This study used the University of Vaasa Advanced Thermo-Kinetic Multi-Zone (UVATZ) combustion model. The model was originally developed by Vasudev et al. [17] for fast predictive simulation of natural gas and diesel-fueled RCCI combustion and accounts for key factors such as fuel and thermal stratification, in-cylinder turbulence, intake valve closing (IVC) temperature, and residual burnt gas composition. The model was recently improved through the incorporation of more accurate CFD-informed fuel distribution and an advanced turbulence model [66], including cross-validation on different engine platforms with a fuel-flexible combustion mechanism [56]. These enhancements were implemented to ensure that the model comprehensively captured the complexities of LTC concepts driven by chemical kinetics.

The current UVATZ parametrization uses 12 zones comprising disc-shaped zones, representing the cylinder head and piston boundary layers, and annular zones capturing bulk inhomogeneity. Heat loss to the cylinder walls, as well as interzonal heat and mass flows, were modeled using gradient-based transport equations. Figure 2 depicts the zonal configuration and interzonal interactions. Details of heat transfer modeling, considered critical for interpreting the results of the present study, are outlined in Section 3.2.

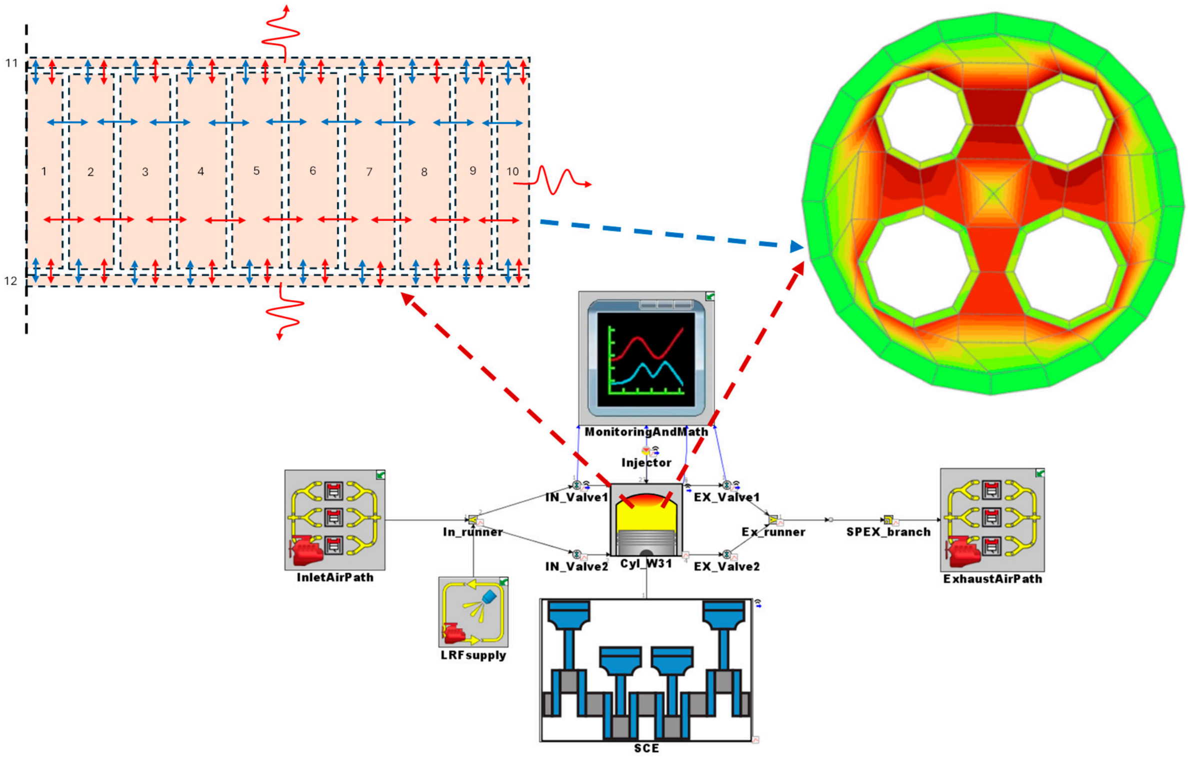

Figure 2. GT-Power 1D Wärtsilä airpath model, including phenomenological illustration of the UVATZ multi-zone model and predictive cylinder wall thermal solver. Note that UVATZ calculates the heat exchange rate with the cylinder boundaries as a sum of three streams (piston, head, and liner) interacting with respective boundary zones 10–12. Small red and small blue arrows are for heat and mass transfer, respectively.

The turbulence effects in the current implementation were captured using a globally valid tuning constant, as outlined in [17]. Chemical reactions are handled using a mechanism accommodating 54 species and 269 reactions, developed by Yao et al. [60]. The stratification of the HRF was described by a simplified injection model, involving case-dependent fuel distribution (refer to Section 3.2 for more information).

The surrogate used for the HRF was defined as n-$C_{12}H_{26}$, while the LRF was defined as a mixture of CH_4, C_2H_6, CO, and N_2. The entire model, implemented in C++, used Cantera thermo-chemical libraries and the CVODES solver [67], requiring approximately three minutes per closed-cycle simulation on an Intel (R) Core (TM) i7-10850H CPU @ 2.70 GHz processor. Further details of the governing equations and modeling assumptions were presented in the work by Vasudev [17].

3.2. The One-Dimensional Engine Model and Model-Coupling Methodology

The one-dimensional model of the reference Wärtsilä Mono SCRE was built using the GT-Suite simulation software v2023 and v2024 [68]. The model was detailed in terms of airpath discretization and, in addition to the standard four-valve layout of the SCRE (as shown in Figure 2), included the complete charge air system and the full exhaust stack.

Figure 2 shows the thermally coupled simulation framework for the Wärtsilä W31 engine, combining detailed in-cylinder thermal modeling with system-level airpath simulation. The top-left schematic illustrates the UVATZ MZM, where red arrows represent heat transfer, and blue arrows denote mass transfer between zones, thereby capturing stratified combustion and wall interactions. The top-right subfigure shows the resulting head temperature distribution, highlighting localized thermal gradients generated by combustion. The bottom section depicts the GT-Suite-based W31 airpath model, including intake and exhaust systems and fuel injection and control components. Due to the absence of a turbocharger, the charge air system model incorporated compressors, buffer tanks, a dryer, and pressure-regulating valves to manage pressure and temperature. A similar level of detail was applied to the exhaust side, which included real pipe geometries from the test cell, a buffer tank, and a regulated backpressure valve. The model's complexity was driven by the requirement for the test cell to emulate the pulsations of the production version of the Wärtsilä 31DF engine, which features different cylinder/turbocharger geometry layouts. The discretization length for all flow components was set to 124 mm and 170 mm in the intake and exhaust paths, respectively [26].

The integration of UVATZ into the 1D engine model was performed using an external cylinder object template available in GT-Suite. To this end, the UVATZ C++ code was compiled as a dynamically linked executable. GT-Suite managed the airpath dynamics and gas exchange, while UVATZ handled the combustion process. UVATZ was controlled by the GT-Suite solver at IVC, using precalculated mixture thermodynamic parameters and composition as inputs. After combustion, at the EVO (exhaust valve opening), the simulation results were transferred back to the GT-Suite solver for streamlined post-processing. Figure 3 depicts the model-to-model interaction and data exchange.

This quasi-static coupling approach allowed for separate solution routines for both models. The simulation time for GT-UVATZ averaged 3.5 min per full cycle on an Intel (R) Core (TM) i7-10850H CPU @ 2.70 GHz processor. Convergence was monitored using IMEP, Pmax, average pressure, and flow rate. Tolerance was set to 1×10^{-2} based on these quantities, and between 10 and 15 cycles were required for the entire model to reach convergence. In the current research, the coupling was extended to accommodate a dynamic solution of the in-cylinder boundaries through a predictive wall thermal solver available in GT-Suite. The details of in-cylinder heat transfer and component temperature modeling are described in the following section. This study applied a separate convergence criterion for the cylinder head temperature to track the convergence of the wall thermal solver.

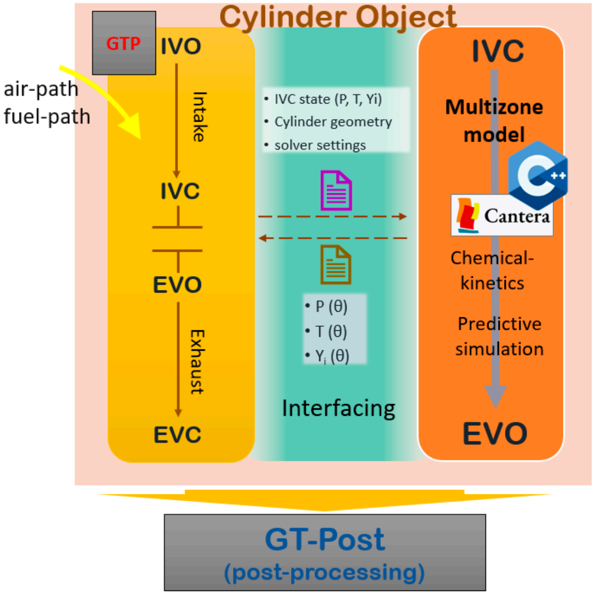

Figure 3. Schematic of data exchange in GT-UVATZ coupling methodology.

3.3. In-Cylinder Heat Transfer Modeling and Predictive Thermal Solver

Due to the quasi-static approach in which the UVATZ code was executed by the GT-Suite master engine model, the in-cylinder heat transfer solution was partially decoupled. In general, gas-side heat transfer was assumed to occur through convection between the cylinder walls, with the heat transfer coefficient modeled using the well-established correlation by Woschni [43], as defined in Equation (1).

$$h_c = CB^{m-1}p^m w^m T^{0.75-1.62m} \tag{1}$$

This formulation considered the influence of in-cylinder pressure (p) and temperature (T). The constant C was used as a calibration parameter, adjusted around the original value of 3.26, as proposed by Woschni [69]. The exponent term m was considered fixed at 0.8. B represented the cylinder bore, and the term w encapsulated the wall-side interaction, as described by Equation (2).

$$w = \left[C_1 \overline{S}_p + C_2 \frac{V_d T_r}{p_r V_r} (p - p_m) \right] \tag{2}$$

The geometrical variables in Equation (2) are as follows: $\overline{S}_p$—the mean piston speed, and V_d—the displacement volume. The subscript r, for the respective thermodynamic properties (p, T, and V), denotes the reference conditions, i.e., the temperature, pressure, and in-cylinder volume at IVC. Finally, p_m is the motoring pressure, i.e., resulting from the compression/expansion, without the combustion term. Equation (1) was also used to calculate the heat transfer coefficient in both the UVATZ model and in GT-Suite.

In GT-Suite, the heat transfer rate was calculated as the convolution of the previously mentioned heat transfer coefficient, bulk in-cylinder temperature, and wall temperature. The wall temperature was discretized into multiple component sections, namely the cylinder head with valves and valve guides; the cylinder block; and the piston, including rings. This was performed at the end of each combustion cycle and was used to post-process the results of the in-cylinder remodel: gross heat release rate (HRR) calculation derived from UVATZ-based in-cylinder temperature and pressure traces.

The UVATZ combustion model, however, calculated the heat transfer with the cylinder boundaries as an inherent part of its solution, along with the interzonal heat and mass transfer. This was resolved into a sum of three streams affecting the boundary zones surrounding the cylinder liner, head, and piston crown. In this case, the gas-side wall temperatures corresponded to these three macro-components and were updated at the beginning of each combustion cycle using the spatially averaged gas-side component temperatures obtained from the FEM solver in the GT-Suite environment. The relevant assumption is illustrated in Figure 3 (combustion model part).

From the perspective of the combustion code, the heat transfer calculation was performed at each time step using the same general equation, Equation (1), but with tuning parameters pre-calibrated such that the heat transfer rate to the individual boundary zones matched the bulk model used by GT-Suite, as discussed above. In practice, this meant that the total heat transfer from the combustion code's perspective (affecting combustion phasing and emissions prediction) was slightly different on a case-by-case basis than that from the wall thermal solver's perspective (affecting element temperatures). However, as both phenomena were relevant to different time scales, this minor inconsistency was considered acceptable for the purposes of the present study.

The cylinder structure of the wall thermal solver was provided as detailed specifications in GT-Suite; the shape of the parts was estimated by GT itself. The components' material properties, such as thermal conductivity and heat capacity, were specified based on the material codes available in the manufacturer's specifications. Table 3 presents the most relevant data from the perspective of thermal solver parametrization.

Table 3. Heat transfer coefficients, initial values, and coolant boundary conditions for the engine cylinder thermal model implemented in GT-Power adjustment for modeling.

Structure to Structure HTR Parameters			Initial Component Temperatures and Boundary Conditions		
Skirt to Cylinder HTR Coefficient	W/(m^2-K)	2500	Head Initial Temperature	K	745
Ring to Piston HTR Coefficient	W/(m^2-K)	15,000	Piston	K	440
Ring to Cylinder HTR Coefficient	W/(m^2-K)	30,000	Cylinder	K	430
Valve to Seat HTR Coefficient	W/(m^2-K)	70,000	Int. Valve 1	K	556
Valve to Guide HTR Coefficient	W/(m^2-K)	10,000	Exh. Valve 1	K	635
Head Gasket Contact Resistance	(m^2-K)/W	1×10^{-6}	Cylinder Coolant Temperature	K	358
Head Gasket Material/Conductivity	W/(m-K)	1.23×10^{0}	Cylinder Coolant HTC	W/(m^2-K)	12,000
Head Gasket Material/Density	kg/m^3	1.00×10^{0}	Head Coolant Temperature	K	353
Head Gasket Material/ Specific Heat	J/kg-K	2,500,000	Head Coolant HTC	W/(m^2-K)	8000
Head Gasket Thickness	mm	2	Coolant to Valve HTC	W/(m^2-K)	3000
Ring/Engine Friction Ratio	[-]	0.25	Cylinder Oil Temperature	K	353
Skirt/Engine Friction Ratio	[-]	0.25	Cylinder Oil HTC	W/(m^2-K)	1000
Head to Valve Contact Resistance	(m^2-K)/W	1.00×10^{-12}	Piston Oil Temp. (Zone 1)	K	333
			Piston Oil HTC (Zone 1)	W/(m^2-K)	10,000

The thermal characteristics of the interfaces between parts were specified as thermal contact resistance. Examples of these interfaces are between the piston ring and cylinder block and between the valve and its seat and guide. Figure 4 illustrates various regions involved in modeling gas-to-structure (GTS) heat transfer in GT-Suite. The diagram depicts various engine components and the heat transfer mechanisms occurring between them.

Arrows represent heat transfer pathways, including gas-to-wall, wall-to-coolant, solid-to-solid, and wall-to-oil interactions. The necessary input data for accurately modeling these heat transfer processes were incorporated into GT-Suite, ensuring proper thermal solver adjustments, as detailed in Table 3. This figure was considered essential for visualizing the heat distribution and validating the thermal modeling approach. The boundary conditions included the temperatures of the coolant in the cylinder block and head and the temperature of oil flowing through the piston gallery. The boundary conditions are specified in Table 3. Heat generated from friction between moving interfaces—primarily between the piston rings and liner—was captured in a simplified manner by defining a ratio between ring friction and total engine friction. This ratio determined the quantity of engine friction imposed as a heat rate boundary condition on the finite element (FE) nodes of the two respective parts. An empirically determined value of 0.25 was selected for this parameter, while total engine friction was predicted using the Chen–Flynn model [69], which was incorporated into the cranktrain component (denoted as SCE in Figure 4).

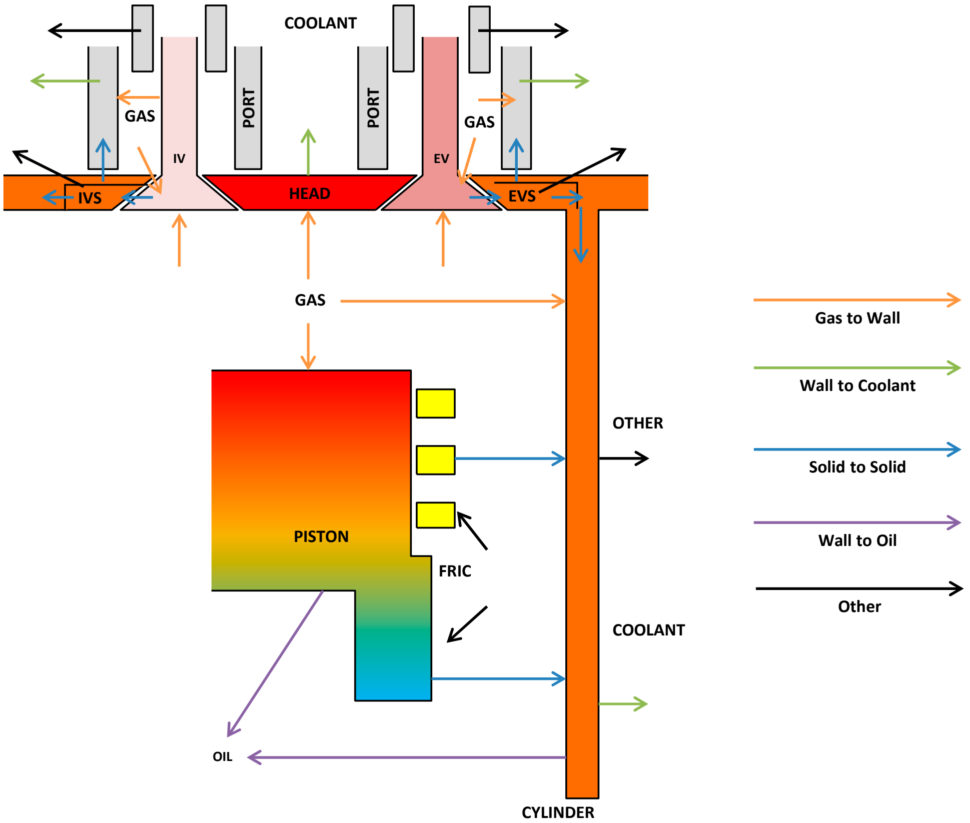

Figure 4. Gas-to-structure (GTS) and structure-to-structure (STS) heat transfer map in GT-Power structural solver.

4. The Scope of the Research

Model Calibration and Validation

The coupled model, as described in Section 2, was thoroughly calibrated in a study by Kakoee et al. [26]. The validation involved the same RCCI engine/combustion reference data as discussed in the present work (Table 2), but the mean value temperatures of the in-cylinder walls were directly imposed from the experimental data. The study confirmed that the coupled model was able to predict all performance parameters within a 3% accuracy threshold, using only engine control unit (ECU) inputs.

RCCI combustion was recognized as highly sensitive to boundary conditions. In particular, the thermal stratification invoked by cylinder heat transfer was considered the second most important phenomenon, after reactivity stratification. The physics-based UVATZ model reproduced this sensitivity, and the inclusion of the predictive wall thermal solver was expected to diverge the simulation results from their nominal, experimentally pre-calibrated values. This inclusion also influenced the model's cycle-to-cycle convergence, as additional degrees of freedom were introduced with dynamically calculated cylinder boundary temperatures replacing imposed values.

Given these considerations, the scope of the present study necessitated a dedicated calibration approach. Three out of six RCCI operating points from the Wärtsilä 31 SCRE test campaign, points B, C, and F from Table 2, were used to re-calibrate the model, now including the thermal solver. These operating points were used for baseline UVATZ–GT model calibration in Kakoee et al. [26]. The remaining three points, A, D, and E from Table 2, were used to validate its accuracy. To address the complexity and manage model convergence time, the calibration procedure followed the steps described below:

(i) Wall thermal solver pre-calibration. In the first calibration stage, the GT-Suite model was initialized using experimentally measured in-cylinder pressures as the combustion object. This meant that the predictive UVATZ model was deactivated to avoid convergence issues that could occur if the predicted component temperatures diverged significantly from the experimental reference. This approach allowed for efficient pre-calibration of the thermal solver to match the experimentally measured temperatures at various cylinder locations (Figure 1). Calibration parameters were selected based on a separate sensitivity analysis performed individually for the cylinder wall, piston deck/skirt, cylinder head, and valves. The spacing between the component element and the cooling jacket was identified as the most sensitive parameter affecting wall temperature and so was calibrated first. This parameter was recognized as difficult to determine rigorously, since the complex cooling channel geometry represented in the sketch drawings of the cylinder cross-section had to be reduced to a mean value in the thermal solver model. To this end, the individual distances were determined in a way that avoided over-cooling of the elements while ensuring that sensitivity between the operating points was captured. Following this procedure, an absolute-level fit between the experimentally measured temperatures for individual component elements was achieved by manually fine-tuning the thicknesses and heat transfer coefficients around their nominal values obtained from the material data sheet. For all component categories, the parameters were adjusted within ±10% of the nominal values presented in Table 3, corresponding to the typical range of production tolerances between components.

(ii) Complete model calibration in terms of combustion characteristics. As the UVATZ model had already been calibrated to take the experimental wall temperature as an input, enabling the predictive combustion feature to be solved together with the calibrated wall thermal solver was expected to result in convergence toward feasible steady-state outputs on both the engine performance and thermal sides. However, differences in the initial conditions and the combined inaccuracies of the predictive models led to some deterioration in the overall accuracy of the coupled model. Therefore, the tuning parameters of the UVATZ model were slightly adjusted around their standalone calibration values to ensure that the model closely resembled real engine operation. The tuning procedure for UVATZ was comprehensively described in Vasudev et al. [17] and Kakoee et al. [26] and so is not thoroughly repeated here. For reference, the reader should note that the UVATZ tuning parameters involve interzonal mixing intensity through the turbulence coefficient, ζ_u, and the liquid fuel stratification parameter, ζ_∇, optimised via an automated procedure to minimise residual error against experimental pressure traces. ζ_u is globally calibrated, while ζ_∇ varies depending on the case [26]. Correction factors for UVATZ coupling with the GT airpath model included IVC temperature, which needed to be slightly elevated to account for the shortcomings of the kinetic mechanism involved [17].

Additionally, as previously mentioned in Section 2, a tuning parameter in the cylinder heat transfer sub-model was employed to ensure consistency between the zonal heat-loss solution and the bulk cylinder temperature model used by GT-Suite. Only globally valid parameters were adjusted during the retuning process, within a pre-defined ±10% range from the previously calibrated setpoints. The objective function was defined as the minimization of the root mean square (RMS) error in in-cylinder pressure. The experimental results for in-cylinder pressure analysis were post-processed using GT-Suite's three pressure analysis (TPA) method [68] to obtain bulk cylinder temperature, cumulative heat release rates (CHR), and combustion indicators such as crank angle at 10% and 50% mass burned (CA10 and CA50). The TPA method, which involved backward analysis from experimental in-cylinder pressure data, also enabled the assessment of engine efficiency indicators and heat transfer losses. Correspondingly, simulation results were post-processed using a forward run in GT-Suite to ensure a consistent benchmark for comparison with experimental values.

(iii) Remarks on emission calibration. UVATZ did not include any separate phenomenological sub-model for emissions. Emissions were calculated in each zone during the resolution of the chemical kinetic mechanism and shared its inherent limitations. To this end, it is important to note that the chemical mechanism by Yao et al. [60] was optimized for heat release estimation and did not incorporate NO_x reaction pathways. As a result, the available emission factors were limited to hydrocarbon emissions (including CH_4 and intermediate hydrocarbons) and CO. Emission trends were predicted reliably due to the physical nature of the model. However, the size of the boundary layer significantly influenced combustion quenching near cold liner surfaces, which contributed to predicted methane slip and CO emissions. By tuning the boundary layer size to the specific engine geometry, UVATZ was shown to capture absolute emission values with a maximum error of 25%. This was demonstrated for a smaller Wärtsilä engine (200 mm bore) and was comprehensively discussed in [66].

It should be noted that adjusting the boundary layer size would ultimately affect the results related to heat exchange with the cylinder wall. Emissions were not the primary focus of the present study, so the model was not re-calibrated separately for emissions. This decision was made to prioritize accuracy in thermal predictions while limiting the calibration burden. In selected case studies discussed in this work, simulated CH_4 and CO results are presented to highlight the significance of the cross-coupling between predictive combustion and the wall temperature solution. Given the limitations described above, the emission results presented in this study should be considered trend-wise accurate, without making claims regarding the absolute emission levels of the simulated engine.

5. Design of Simulations

After the model validation was confirmed against the experimental data (Campaign 0), the investigation continued with selected model-based case studies aligned with the predefined research objectives. These case studies were centered around the governing thermal management challenges of RCCI, particularly in the context of load extension. Accordingly, they were established at boundary operating points of 25% and 85% rated power—corresponding to cases B and E in Table 2, respectively. It should be noted that 85% load represented the practical limit for efficient RCCI operation on the current engine hardware, as combustion became limited by excessive pressure rise rates (PRRs). Table 4 summarizes the research objectives of each case study, along with the details of the corresponding simulation experiment designs.

Table 4. Simulation campaigns considered in this study, along with objective speciation and swept parameters. Reference conditions (ref B/ref E) relate to corresponding experimental setpoints provided in Table 2.

Campaign	Load/Case	λ [–]	BR [pp]	T_{cool} [K]	T_{pist_oil} [K]	Investigation Objective
Campaign 1	10–83% Case A–E	According to Table 1		358	333	O1. Validate the new framework using comprehensive experimental data.
Campaign 2	25% Case B	ref B	ref B			O2. Benchmark component thermal loading at different RCCI operating conditions.
	83% Case F	ref F	ref F			
Campaign 3	25% Case B	ref B	ref B	318–418	333	O3a. Determine the sensitivity of RCCI combustion to wall temperature, considering spatially diversified heat transfer paths.
				358	313–373	O3b. Examine the feasibility of coolant and oil circuit temperature control for reducing methane slip at low engine loads.
Campaign 4	83% Case F	−0.2 ref F +1	−0.34 ref F +0.31	358	333	O4a. Determine the sensitivity of wall temperature to RCCI operating conditions. O4b. Examine the feasibility of coordinated airpath–combustion control for reducing thermal stress during high-load RCCI operations.

In the first campaign, both cases were benchmarked for detailed component temperature distribution in the context of operational tolerances. The discussion focused on understanding the phenomena responsible for case-to-case differences in thermal loading. As low-load RCCI operation was constrained by methane slip [70], the second campaign investigates increasing the coolant and oil circuit temperature as a means to reduce the flame quenching near the cylinder boundaries. Note that in the given engine design, the oil was particularly used to cool the piston crown, while the sensitivity to oil temperature for other components was an order of magnitude lower compared to the cooling effect invoked by the coolant. As the thermal solver allowed us to specify separate temperatures for different parts of the oil-cooling circuit, only the piston oil temperature (Tpist_oil) was varied in the sweep. To this end, both lube oil and glycol temperatures are varied from nominal values at 333 K and 358 K, respectively, up to their boiling margins. Two backward sweep points (reducing the temperatures) were added to each of the cases for a consistency check. Other parameters of the simulation are unchanged with respect to the baseline operating point, B. The cause-and-effect investigation involved tracking the temperatures of relevant engine components and their effects on simulated combustion and emissions.

The coolant temperature adjustment, hypostasized in campaign 3, as an effective measure to reduce methane slip, is considered a global measure for most engine applications; i.e., active control of the coolant circuit temperature, available for research engines, like the one used in this work, is rarely a feature available for production engines. Adjusting the thermostat for higher coolant temperatures (passive/hardware measurements) would ultimately limit the high-load engine operation by exceeding the thermal stress limits of the individual cylinder components. In this context, campaign 4 explores the potential of reducing the component temperature by means of active combustion control. Simulations were designed around the high-load case, E. Mixture dilution was selected as a measure to reduce the combustion temperature, and its effects on heat transfer and component temperature were investigated at a fixed coolant/lube oil temperature. The mixture dilution sweep was realized by means of combined lambda (air/fuel ratio) and combustion phasing control; i.e., at a fixed total fuel energy input, intake pressure was elevated to reach the desired lambda at each point of the sweep. The range of the lambda sweep was chosen such that it explored the limits of a contemporary charging system, varying the charge air pressure from around 5 bar to 6.5 bar. Changing the lambda at fixed fueling setpoints heavily affects the combustion phasing, deteriorating the indicated efficiency. To make the case study feasible, the combustion phasing was actively controlled in the simulation by adjusting the blend ratio between the high- and low-reactivity fuel.

6. Results and Discussion

6.1. Validation of the In-Cylinder Wall Thermal Solver

Figure 5 presents two subplots, corresponding to the successive steps of the calibration process. Figure 5a shows wall temperature calibration results, assuming direct experimental burn rates imposed as the combustion object via three pressure analysis (TPA). A total of 81 points were plotted, corresponding to three validation cases—Case B, Case C, and Case F—representing an engine load sweep from 21% to 83% (Table 2). Figure 5 compiles 27 results for each operating point. These represent the individual measurement locations illustrated in Figure 5: 10 for the cylinder head, 6 for the liner, 5 for the piston crown, and 3 for each of the representative exhaust and intake valves. Figure 5b compiles the same set of results, but in this case, combustion was predicted by the UVATZ code rather than being directly imposed.

In Figure 5a, representing the GT-TPA reference simulation, the largest deviations occur at the intake and exhaust valves, where individual points show errors reaching ~7%, although this happens only at one operating condition and on one point. For all other components, and for most valve points, deviations remain below 5%, consistent with the overall accuracy of this 1D model. The cylinder head, liner, and piston markers lie close to the 1:1 line, indicating good agreement with measurements, whereas the valve markers (green and purple) diverge more noticeably. These higher errors stem mainly from the valves' complex geometry and the influence of scavenging flow, which create localized heat transfer conditions that are difficult to capture with a simplified model. Improving the representation of these effects is expected to further enhance valve temperature predictions.

In Figure 5b, which represents the GT-UVATZ simulation, a clear improvement in the clustering of data points around the diagonal line is observed, indicating better agreement between simulated and experimental results. The intake and exhaust valve markers are positioned closer to the diagonal line compared to Figure 5a, highlighting the enhanced accuracy of the GT-MZM model in predicting temperatures for these components. Moreover, GT-TPA, Figure 5a, shown a deviation of more than 8%. This improvement was attributed to the multi-zone modeling approach, in which the combustion chamber was divided into multiple zones, each with distinct thermodynamic properties. This method enabled a more effective capture of spatial temperature variations, resulting in more accurate predictions of heat transfer and temperature distributions across various engine components, particularly in complex regions such as the valves.

Importantly, the validated model predicted wall temperatures with a maximum error of 10 K, and the average error across all operating points and components did not exceed 2% for most data points. It should be noted that the mentioned 10 K error was close to the measurement uncertainty, considering transducer characteristics, tolerances in sensor mounting, and variability in combustion conditions. In particular, the actual distance between the thermocouple and the corresponding simulation surface was subject to stochastic variation, influenced by uncertainties in machining depth and the thickness of adhesive layers. In comparison to these stochastic effects, the transducer error was an order of magnitude lower, especially in higher temperature ranges, where sensor error was limited to approximately 0.5%. The transducer error became negligible for colder engine components. Given the experimental uncertainty described above, it could be concluded that the phenomenological simplifications in the gas-to-surface heat transfer model were irrelevant within this context. Therefore, the model was considered suitable for predicting thermal loading of RCCI engine components, using only ECU (engine control unit) control parameters as input.

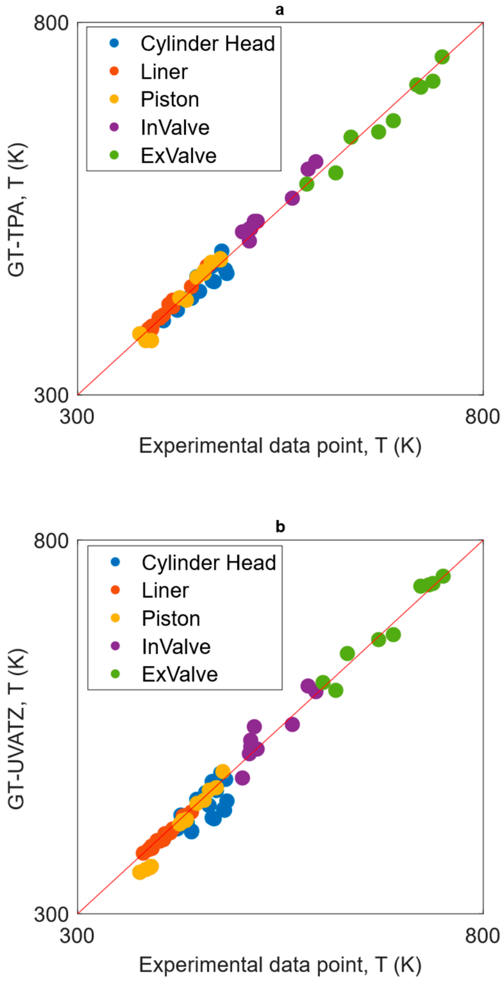

Figure 5. Point-to-point temperature comparison of simulated and experimental component temperatures for three different load points (Case B, Case C, and Case F). (**a**) Calibration results with imposed experimental burn rate (TPA); (**b**) full model validation including predictive combustion model (UVATZ).

6.2. Combustion Modeling Accuracy with Predictive Wall Thermal Solver

The UVATZ combustion model had already been calibrated to the corresponding area-averaged values of experimental wall temperatures, as presented in Figure 6, in the earlier study by Kakoee et al. [26], which considered imposed experimental temperatures as inputs. Due to the high sensitivity of RCCI combustion to thermal stratification, even a small 2% error in wall temperature estimation could lead to substantial differences in the prediction of combustion parameters. To prevent the accumulation of such errors, the combustion model was re-calibrated to minimize discrepancies when component temperatures were dynamically calculated. To verify the accuracy of this approach, Figure 6 presents the results of the relevant simulated and experimentally post-processed combustion parameters, obtained via TPA. The validation results correspond to the same three operating points, as discussed in the previous section, for consistency.

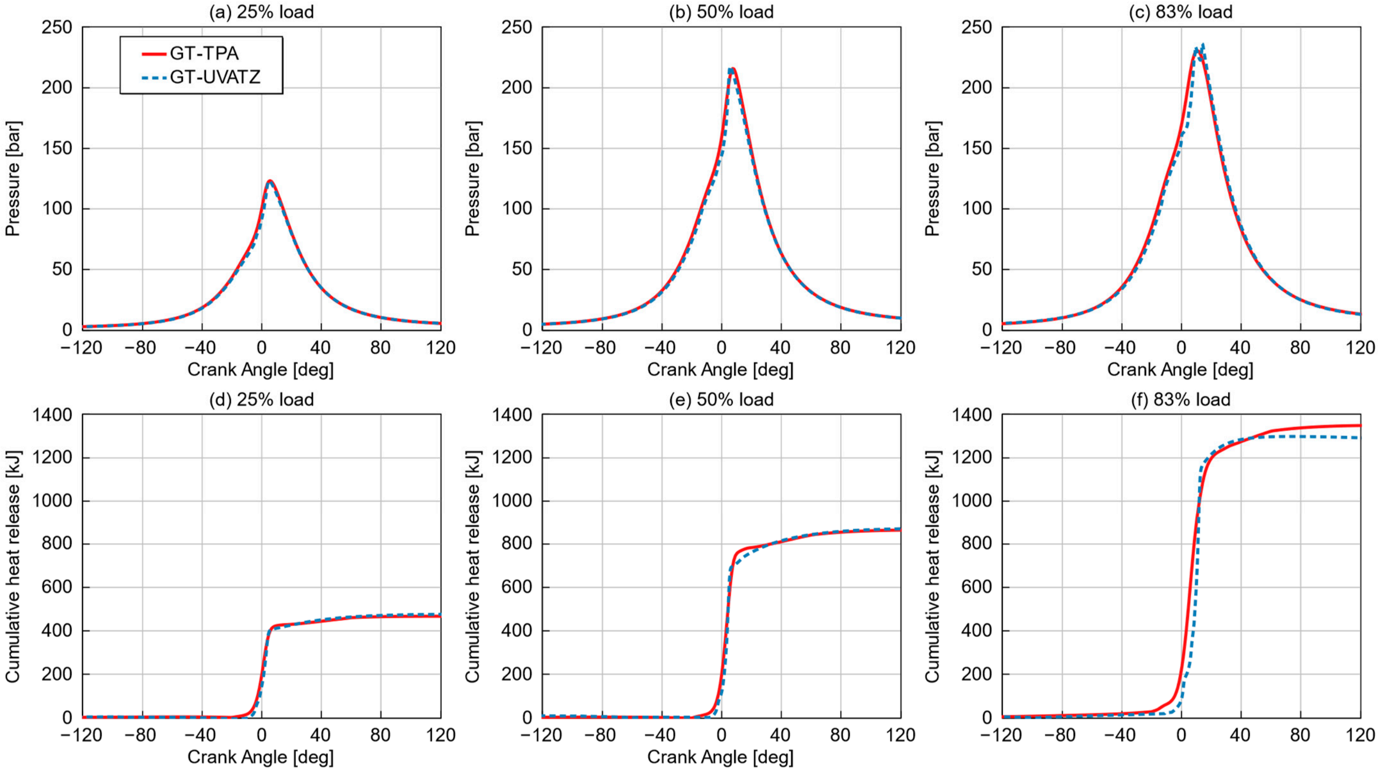

Figure 6. Pressure and cumulative heat release (CHR) simulated in GT-UVATZ compared with experimental data (TPA); Cases: (**a**,**d**) B—25% load; (**b**,**e**) C—50% load; and (**c**,**f**) F—83% load. Absolute errors in relevant combustion indicators are provided on the CHR plots for each case.

Focusing on low engine load, Figure 6a shows that the UVATZ-predicted pressure trace closely matches the experimental reference. In particular, the start of combustion and the peak pressure were captured accurately. However, the quality of the fit deteriorates with increasing load. It should be noted that overall mixture reactivity decreased with engine load, as the amount of injected diesel remained relatively small (i.e., low blend ratio (BR) values) and was significantly diluted due to increased intake pressures. Under such conditions, adjustment of HRF distribution and turbulence levels alone—the primary tuning parameters—proved insufficient for enabling reliable auto-ignition reactions. Because only a limited quantity of diesel was available for distribution within the coarse 12-zone configuration of the model, UVATZ required an additional correction factor applied to the IVC temperature to ensure agreement between the simulation results and experimental data. For high-load operation (Case F), the IVC temperature had to be elevated by nearly 10% compared to the experimental reference in order to achieve acceptable results. As mass was conserved within the cylinder, this introduced temperature correction resulted in a slight underestimation of pressure during the compression stroke, as evident in Figure 6c. The magnitude of this effect diminished in all lower-load cases.

Several studies support the physical basis for the required high-load IVC temperature correction. Cho et al. demonstrated that intake and exhaust valve temperatures increase disproportionately at high load due to backflow and intensified valve heat flux, effects that 1D airpath models typically underpredict [12]. Kokjohn et al. further showed that high-load RCCI operations become highly sensitive to boundary-condition errors, particularly charge temperature at IVC [13]. These findings substantiate the load-dependent deviation observed in Case F and confirm that the applied correction is physically motivated rather than empirical.

The same trend was observed in the original UVATZ–GT-Suite coupling tested by Kakoee et al. [26]. However, the present implementation allowed the required IVC temperature correction to be reduced by half, highlighting the importance of accurately resolving wall temperatures. This outcome was understandable, as RCCI combustion is known to exhibit very high sensitivity to in-cylinder thermal stratification induced by heat loss to cylinder walls [27].

Turning to the CHR plots in Figure 6, the start of combustion is predicted reasonably well across all validation cases, with the error in CA10 not exceeding 2 CAD. This was considered acceptable, given the high sensitivity of RCCI to both thermal and reactivity stratification. Importantly, the simulated CA50 remains in close agreement with the experimental reference across all operating points. As discussed in Section 3.2, the UVATZ model relied on continuous fuel distribution among zones to achieve a realistic combustion sequence. Due to the limited number of zones constraining the formation of highly reactive regions, the trade-off between CA10 and CA50 was considered unavoidable. However, since CA50 directly influenced how the simulated combustion translated into engine performance, the ability to predict this parameter accurately was essential from the standpoint of performance analysis.

Despite the above, the overall combustion process was captured well. The RMS error in CHR reproduction remained below 2% for all cases analyzed. In the RCCI regime, this level of accuracy was recognized as particularly challenging to achieve, even for significantly more computationally intensive, high-fidelity 3D CFD models [56]. Importantly, the total amount of released energy, reflected by the saturation level of the CHR curve, was predicted with even lower error, below 1.5%. This parameter was directly influenced by two factors critical to the current study: the quantity of unburned hydrocarbons and the total heat loss through in-cylinder walls. For the sake of brevity, these parameters will not be discussed separately in the validation section but will be elaborated upon during the analysis of subsequent simulation campaigns. At this stage, it is sufficient to note that the high accuracy in net heat release confirmed the validity of the calibration approach with respect to emission trends. As previously mentioned in Section 2, emissions were not retuned in order to manage the complexity of the calibration process.

6.3. Relevant Engine Performance Indicators

Figure 7 presents the validation results of the GT-UVATZ model developed for thermal loading analysis by comparing relevant engine-out parameters. These results expand on the crank-angle-based analysis reported in the previous section by including corresponding results related to the engine fuel/airpath and friction modeling. The parameters analyzed included indicated power (IP), air flow rate (AFR), indicated specific air consumption (ISAC), indicated specific fuel consumption (ISFC), volumetric efficiency (VE), trapping ratio (TR), air-to-fuel ratio (A/F ratio), indicated thermal efficiency (ITE), maximum pressure (Pmax), and net heat release rate (NHR). These specifications were recorded in the GT-Post environment and were benchmarked against reference experimental data for validation. The results demonstrated that all engine output specifications had deviations of less than 5% from the reference data across all load conditions. The most significant deviations were observed at high loads (Case F), particularly for IMEP at 720° (IMEP720), ISAC, ISFC, and ITE, suggesting higher sensitivity to operating conditions at elevated loads. This was a direct manifestation of the inaccuracies in in-cylinder pressure reported in Figure 7. Conversely, parameters like TR and VE show consistently low deviations across all cases, indicating high predictive capability for the airpath model.

https://doi.org/10.3390/en19010083

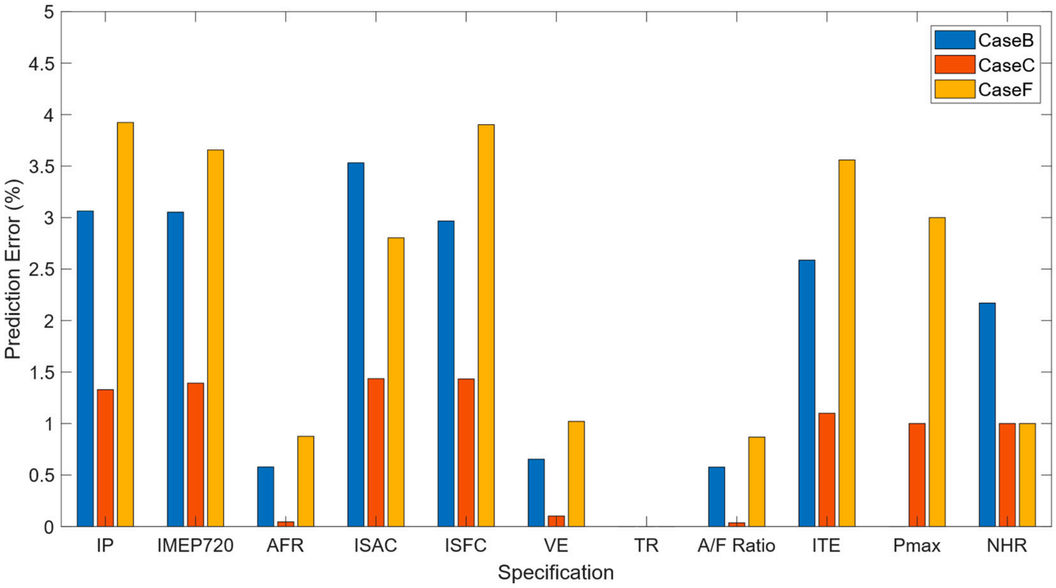

Figure 7. Relative error in simulated engine performance parameters: Cases B, C, and F.

Concluding the discussion of Figures 6 and 7, the governing takeaway is that the predictive wall thermal solver improved the performance of the UVATZ model by reducing its dependency on IVC temperature tuning. This, in turn, benefited the accuracy of reproducing in-cylinder pressure and all indicated specific values. Conversely, the discretized gas temperature in UVATZ enhanced the accuracy of the connected FEM thermal solver. The accuracy of component temperature calibration was found to be, on average, 10% better than the two-zone approach used in GT-Suite's standard combustion model (TPA). At the same time, the results indicated further potential for improvement, either by (i) increasing the zonal resolution of UVATZ or (ii) re-calibrating the chemical kinetic mechanism. It should be noted that the chemical mechanism used in this study was not developed specifically for LFO, which may explain the observed deficiencies in ignition behavior. These improvement suggestions are considered relevant for further development of the simulation toolchain but ultimately did not limit the model's predictive capabilities in relation to the primary objectives of the present study.

6.4. Thermal Loading of Engine CYLINDER Components in RCCI Combustion Regime

This section investigates the results related to the thermal loading of the selected engine model (W31 SCRE) operating in RCCI mode. The focus is on low- and high-load conditions (Cases B and F), as these operating points are considered particularly challenging for the RCCI combustion regime due to methane slip at low load and thermal/mechanical durability concerns at high load. Detailed analysis was carried out individually for relevant component sections, starting with the piston crown and cylinder head, then the valve components, and concluding with the liner and piston rings. These components differed in material properties and in their exposure to cooling agents.

6.5. Piston Crown and Cylinder Head

Figure 8 illustrates the temperature distribution for the piston section and cylinder head under low-load (25%) and high-load (83%) conditions. Temperatures increased significantly under high load, in both the piston and cylinder head, particularly around the combustion chamber edges and near the exhaust valve regions, where temperatures reached up to 650 K.

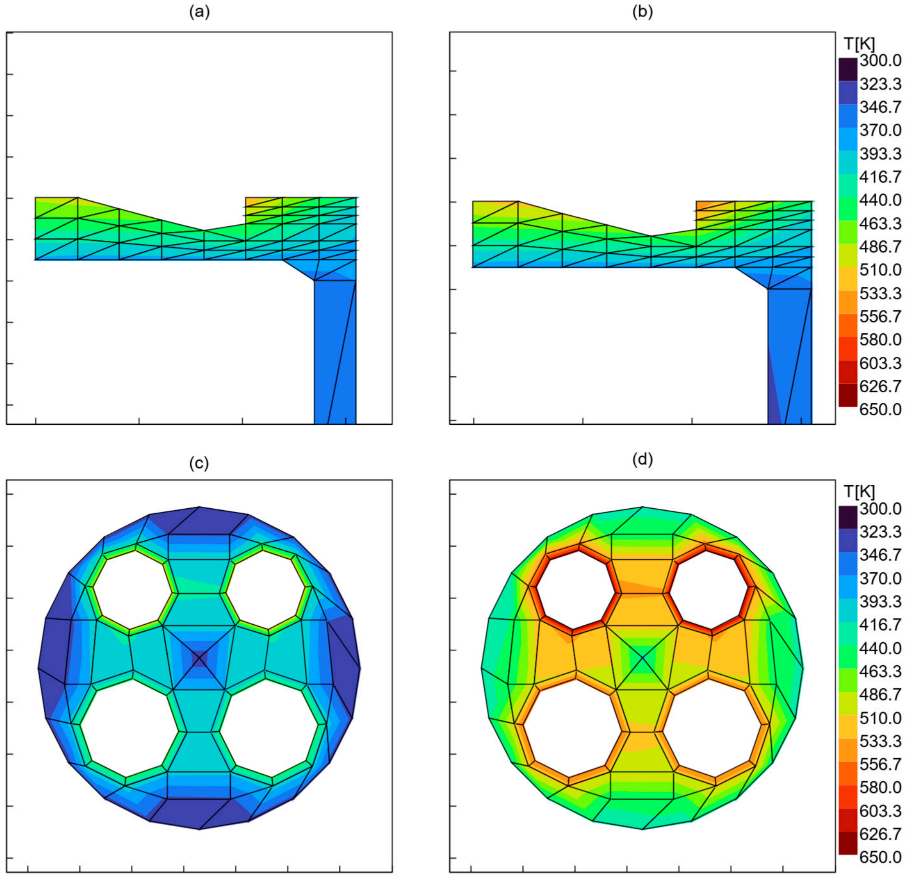

Figure 8. (**a**,**b**) Piston section temperature distribution for low- and high-load cases, Case B and Case F, respectively; (**c**,**d**) cylinder head temperature distribution for low- and high-load cases.

According to the heat transfer characteristics of RCCI combustion, the increase in charge uniformity under low-temperature conditions made the global and local temperature distribution inside the cylinder more controllable and limited elevated local temperatures near the piston and cylinder walls [71–73].

The elevated temperatures near the exhaust valves were attributed to two primary factors. First, the exhaust gases exiting the combustion chamber were at significantly higher temperatures than in other regions of the engine due to the combustion process and energy release, resulting in increased thermal exposure near the exhaust valves. Second, the availability and effectiveness of coolant in this region were lower than in other areas, such as the intake side, where cooler, fresh air entered the system. This combination of intense heat from exhaust gases and limited cooling led to higher localized temperatures near the exhaust valves.

The temperature distribution results were found to be in good agreement with the experimental measurements shown in Figure 8, as areas near the exhaust valve demonstrated relatively high temperatures and corresponding heat accumulation. This phenomenon was also influenced by the substantially higher heat transfer coefficient (HTC) between the hot exhaust valves and the valve seat on the cylinder head side, as detailed in Table 3.

The elevated HTC in this region resulted from the direct metal-to-metal contact between the valve and seat, enabling efficient heat conduction from the hot exhaust valve to the surrounding cylinder head material. Additionally, both the exhaust valve and the valve seat were exposed directly to high-temperature exhaust gases during combustion and the subsequent exhaust stroke. Unlike other engine components that experienced intermittent thermal exposure, these components remained in continuous contact with the hot gas flow throughout the combustion and exhaust phases, resulting in localized thermal stress and elevated surface temperatures. This combination of high HTC and continuous exposure to extreme thermal loads further explains the higher temperatures observed in this region. However, the elevated temperatures near the exhaust valves also enhanced fuel vaporization and mixing, potentially leading to more efficient combustion. Nevertheless, such high thermal conditions pose risks to the integrity of engine components, pushing them closer to their operational temperature tolerances. This could lead to issues such as thermal fatigue, increased material wear, or even premature component failure if not properly managed through adequate cooling strategies [57]. High temperatures were shown to contribute to plastic deformation and asperity fatigue on engine component surfaces, ultimately leading to increased wear [74].

Under low-load conditions, the piston and cylinder head exhibited lower temperatures, particularly around the liner areas. This effect was especially evident in the cylinder head, where temperatures around the liner fell below 320 K, approximately 50 K lower than those observed in the high-load case. These conditions created an environment conducive to flame quenching, where the flame was extinguished near the cooler walls before combustion was completed. Flame quenching was recognized as a significant issue because it led to incomplete combustion and elevated emissions of unburned methane (CH_4), a potent greenhouse gas. Research has shown that low wall temperatures in lean-burn engines are closely associated with increased CH_4 emissions, as cooler surfaces inhibit proper flame propagation near the cylinder walls, resulting in unburned fuel entering the exhaust stream [75].

Contrary to the cylinder head, piston temperature distribution showed considerably lower sensitivity to engine load. The peak temperatures at the piston crown remained within the same range (530–550 K) under both load cases. Differences were observed in the spatial distribution of temperature, with elevated-temperature regions penetrating deeper into the piston crown structure under high-load conditions.

It should be noted that the piston, unlike the cylinder head and liner, was not directly exposed to the coolant circuit. Instead, engine lube oil splash cooling [76] served as the primary thermal management mechanism. This was evident from the piston skirt temperatures, which saturated around the imposed lube oil temperature. The lower sections of the piston remained almost completely insensitive to load. This was as expected because these regions were not directly exposed to combustion. Piston skirt temperature depended more on frictional heat transfer, which was primarily influenced by engine speed [76].

At this point, it is important to note the limitations of the model. The piston gallery, with its complex oil-flow phenomena, was not explicitly modeled in GT-Suite. This is evident in Figure 8, where the simplification had a significant impact on the predicted temperature gradients on the oil-circuit side. Gas-side temperatures were well calibrated to the experimental results (Figure 5), but the oil-side piston temperatures should be considered indicative only. Drawing qualitative conclusions on the piston temperature gradient toward the oil side would require more fundamental CFD simulations, such as the method proposed by Apaydın and Doner [76].

6.6. Intake and Exhaust Valves

Figure 9 shows the temperature distribution around the intake and exhaust valves under the same boundary conditions discussed in the earlier section. The engine was configured with a four-valve layout, including dedicated intake valves designed to promote swirl and tumble. These intake valves had slightly different intake port geometries, which, in real-world conditions, would influence the results to some extent. Due to the simplification applied in the model's port geometry, both intake valves were assigned identical temperature distributions. The surfaces in direct contact with the intake flow heated up to approximately 680 K. The temperature gradient across the intake valve reached 380 K during high-load operation, with the valve stems exhibiting the lowest temperatures.

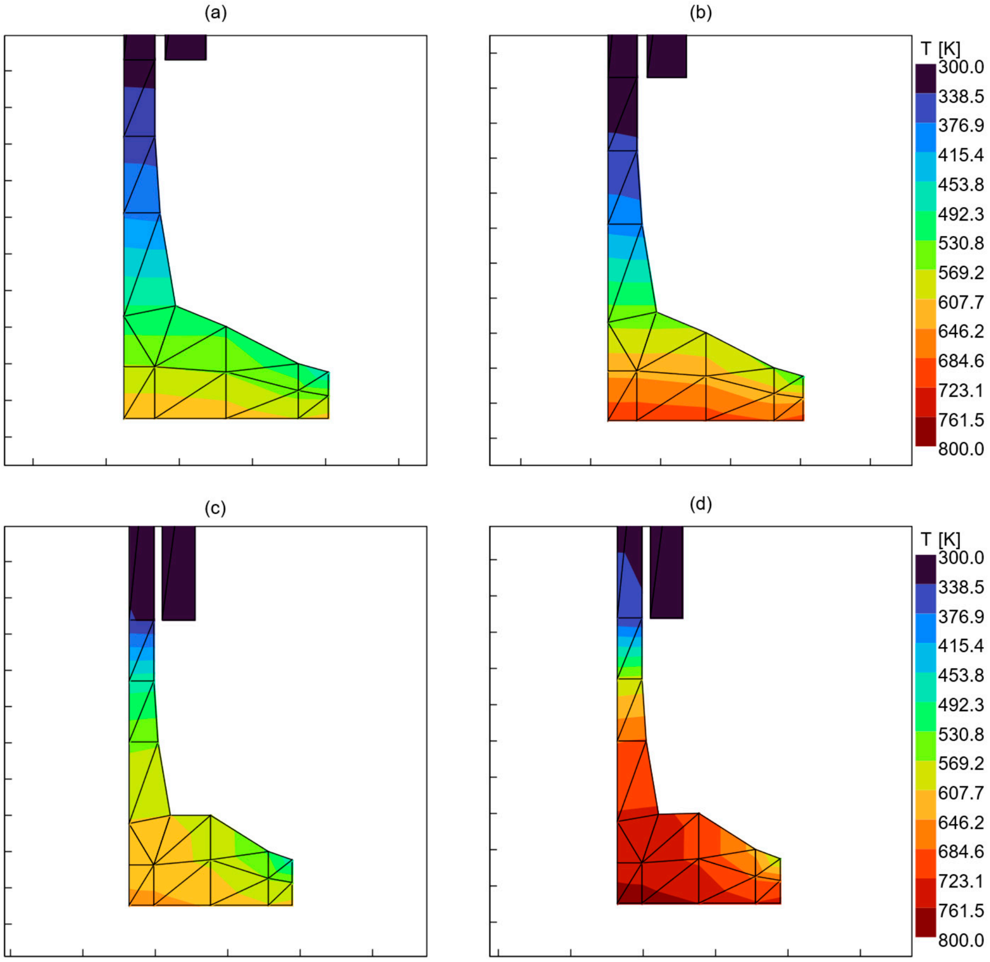

Figure 9. (**a**,**b**) Intake valve temperature distribution in low- and high-load cases; (**c**,**d**) exhaust valve temperature distribution in low- and high-load cases.

The exhaust valves exhibited significantly higher temperatures, especially under high-load operation, where the peak temperature reached approximately 790 K (Figure 9d). This elevated temperature was attributed to direct exposure to hot exhaust gases during the gas exchange process. Such thermal conditions could lead to thermal stresses, material fatigue, and increased wear over time. The highest temperature difference in the high-load case was observed to be about 500 K, as shown in the exhaust valve temperature distribution in Figure 9. The substantially higher HTC for the valve-to-seat interface, combined with the lower HTC between the valve and the coolant (as indicated in Table 3), suggested heat accumulation within the valve structure. The valve stem contributed to heat transfer primarily through conduction from the valve and additionally through the valve guide, but with a relatively low heat transfer ratio. This resulted in decreased temperatures in the stem section of the valve [77].

Effective management of valve temperatures was considered essential for optimum engine performance and emission control. The intake valves, while exhibiting lower peak temperatures than the exhaust valves, still experienced noticeable heating under high-load conditions. This could increase the temperature of the incoming air–fuel mixture, thus affecting combustion dynamics in RCCI operation [78,79].

If high exhaust valve temperatures are not adequately managed, they could lead to increased nitrogen oxide (NO_x) emissions due to locally elevated combustion temperatures.

Notably, in the high-load case, the valve operated just below the auto-ignition temperature of methane (810 K): any carbon deposits, oil residues, or localized hot spots could trigger pre-ignition [80].

This phenomenon was confirmed during the experimental campaign supporting the present study, which identified the 83% load point as the upper limit for stable RCCI operation. The insights provided by Figure 9 are particularly pertinent when considering the potential for hydrogen admixing into natural gas, an attractive strategy for achieving fuel-flexible decarbonization in marine engines.

On the one hand, the RCCI mode offers favorable control strategies to accommodate changes in fuel reactivity resulting from variable hydrogen blend ratios [81]. On the other hand, from this study's perspective [24], even a small hydrogen admixture would substantially limit the permissible engine load. Hydrogen is significantly more prone to auto-ignition than methane because it has an auto-ignition temperature as low as 710 K [82], so this study has identified exhaust valve thermal management as a key enabler for fuel-flexible RCCI engines [24].

6.7. Cylinder Liner and Piston Rings

Figure 10a,b show a clear temperature gradient, with lower temperatures at the bottom of the liner and higher temperatures toward the combustion chamber. The liner reached temperatures of approximately 580 K near the top when under high-load conditions, indicating increased thermal stress in regions closer to the combustion zone. In contrast, the piston rings (Figure 10c,d) exhibited more uniform temperature distributions. However, high-load operation increased ring temperatures, with values peaking at around 561 K. The challenges implied by these temperature variations include increased thermal expansion, particularly in the liner and piston rings under high-load conditions. This could lead to increased blow-by and potential oil film degradation, both of which would negatively affect engine efficiency and emissions. Effective cooling strategies are considered necessary to mitigate these issues, such as improved coolant circulation in the liner or the use of advanced materials with superior thermal conductivity [83].

Figure 11 shows that the portion of the liner directly exposed to the combustion chamber remained considerably hotter than the adjoining head elements (Figure 11). The contact surface temperature difference between the liner and the head at high load was observed to be nearly 100 K, and it became even more pronounced under the low-load operation. This implied that the cylinder head region could contribute more significantly to methane slip than the liner-adjoining zones. However, it should be noted that the crevice zones remained relatively cold, even during high-load operation. Under such conditions, the upper piston ring and lower sections of the liner exhibited similar gas-side temperatures, not exceeding 430 K. This indicated that chemical reactions within the crevice were virtually impossible, and fuel trapped in this region during combustion and released during scavenging would contribute to methane slip. Given the low temperature levels, the only feasible method to reduce unburned hydrocarbon emissions originating from crevices was identified as the addition of a scraper ring. It should be noted that this solution is implemented in the production version of the Wärtsilä 31DF engine, but the prototype RCCI configuration considered in the present study did not include this feature.

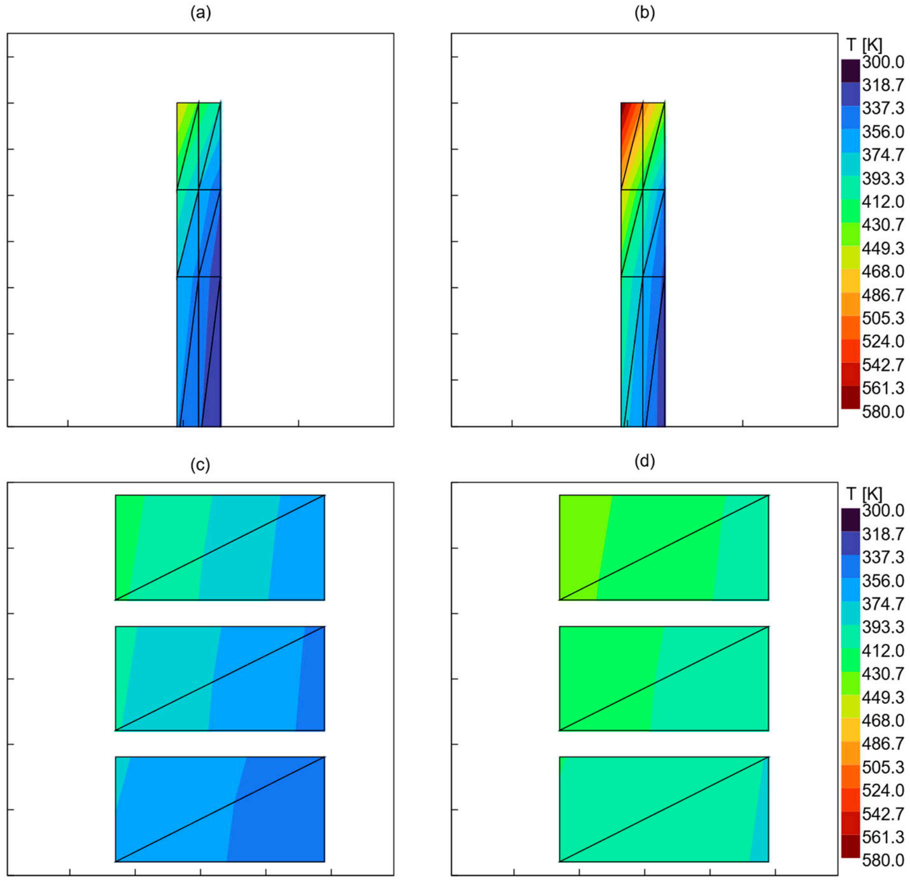

Figure 10. (**a**,**b**) Liner upper section for Case B and Case F, low- and high-load, respectively; (**c**,**d**) ring temperatures for low- and high-load cases, Case B and Case F. Horizontal lines on the liner correspond to piston crown position at TDC (upper) and at +/−10 CA bTDC (before top dead center).

6.8. Heat Transfer Analysis

This study examined the characteristics of heat transfer between the gas, structure, and coolant under varying engine loads to investigate thermal efficiency and energy utilization across different operating conditions. The ratio of high-load-to-low-load gas-to-structure (GTS) and high-load-to-low-load structure-to-coolant (STC) heat rates was quantified.

(a) shows the GTS heat transfer at high load was found to be approximately 1.8 times greater than that at low load, indicating a substantially higher amount of heat produced and transferred to the engine structure under increased load conditions. Conversely, the STC heat transfer ratio for high load relative to low load was approximately 1.65:1, implying a reduced rate of heat rejection from the structure to the coolant at high load.

This decrease in heat absorption by the coolant, despite consistent engine speed, suggested a notable reduction in cooling efficiency under high-load operation. Additionally, the ratio of STC to GTS heat transfer was evaluated under both high- and low-load conditions. The calculated values of this ratio were found to be less than one, emphasizing that a greater proportion of heat was transferred from the gas to the structure than was rejected from the structure to the coolant. Notably, this ratio was significantly higher under low-load conditions, while under high load, it dropped as low as 0.8:1. This underscores the increased thermal loading on the engine structure in the high-load case.

The in-cylinder heat transfer in the predictive thermal solver was found to be greatly influenced by the HTC, as the temperature difference alone was not sufficiently pronounced to cause a substantial variation in heat transfer. This was due primarily to the assumption of constant coolant temperature, given that the engine in this study was assumed to operate in constant-speed mode. Convective heat transfer was modeled using the well-known

Woschni correlation (Equation (1)), as explained in Section 3.3. This relation considered the influence of in-cylinder pressure and temperature, a wall-side interaction term, constant parameters reflecting the geometrical characteristics of the engine, and calibration multipliers. The relationship between average gas velocity, pressure, temperature, and HTC under both high- and low-load conditions was extracted and is illustrated in Figure 11, providing deeper insight into the contributions of these parameters to the thermal differences in the studied RCCI engine with the wall solver.

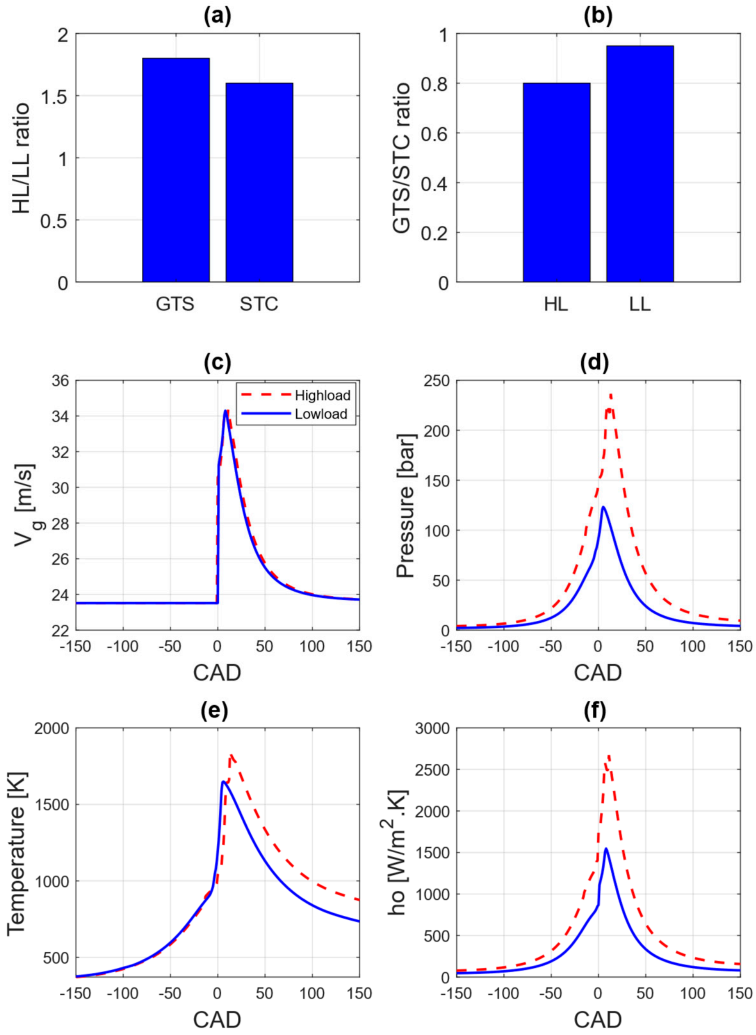

Figure 11. (**a**) High load (HL)-to-low load (LL) ratio for gas-to-structure (GTS) and structure-to-coolant (STC) heat rates; (**b**) structure-to-coolant (STC)-to-gas-to-structure (GTS) heat rate ratio for high- and low-load cases; (**c**) cylinder average gas velocity; (**d**) pressure; (**e**) temperature; (**f**) convective heat transfer coefficient.

The variation in gas pressure and temperature with crank angle degree (CAD) under different load conditions confirmed the direct influence of increased pressure and temperature on HTC. As expected, higher loads led to higher gas pressure and temperature, which in turn increased gas-to-structure heat transfer. The average gas velocity was also correlated with piston speed [10].

In more detail, Figure 11c depicts the impact of gas velocity on convective HTC, despite only marginal differences between high- and low-load conditions. The variations in temperature, pressure, and gas velocity—three of the most influential combustion parameters determining instantaneous HTC—were analyzed over CAD. At high load, peak gas velocity remained approximately the same, while pressure was significantly higher around TDC, resulting in elevated peak gas temperatures above 1800 K, compared to below 1600 K under low load. These elevated pressure and temperature conditions produced increased heat transfer, peaking at approximately 2600 $W/m^2{\cdot}K$ under high load versus 1600 $W/m^2{\cdot}K$ at low load. These differences indicate greater thermal and mechanical stresses under high-load operation, as reflected by the wide span of thermal variation in RCCI combustion.

7. Improving RCCI Operation at Low Engine Loads by Cylinder Thermal Management

The results discussed in the previous section support the hypothesis that globally and locally diluted air–fuel mixtures, which are typical of the RCCI regime, led to reduced heat transfer rates (Figure 6), particularly under low engine load conditions. This resulted in over-cooling of engine components, especially in the cylinder head sections adjoining the liner (Figure 10). These locally overcooled regions were shown to cause kinetic reactions to slow down or, in some cases, not initiate at all [27] in the cylinder zones directly adjacent to these components. This high sensitivity to thermal effects highlights the importance of cylinder component thermal management as a potential optimization and control strategy for improving RCCI performance and emissions under low-load operation.

It should be noted that RCCI naturally counteracted the aforementioned negative thermal effects by establishing a positive reactivity gradient across the cylinder centerline, with most of the high-reactivity fuel concentrated near the cylinder walls [82]. The effect of component temperatures on engine performance and emissions, particularly CH_4, was recognized as a multidimensional problem, involving reaction kinetics in combination with gradient-induced interzonal heat and mass transfer, all within the geometrical constraints of the cylinder liner, piston, and head.

The kinetic-based multi-zone structure of the UVATZ code, when combined with the FEM-based wall thermal solver, provided the required predictive capability while maintaining fast execution times. This makes it a suitable tool for exploring the interactions between wall temperature and combustion phenomena.

The effects associated with RCCI low-load thermal management are assessed in the following subsections, which discuss the two independent cooling circuits. The first of these is the coolant predominantly affecting the head and liner; the second is the lube oil, the main mechanism for cooling the piston crown.

7.1. Effect of Coolant Temperature

Figure 12 presents the results of the coolant temperature sweep conducted around the baseline 25% load condition (Case B). The boundary condition parameter, the cylinder coolant temperature (as defined in Table 2), varied around the baseline setpoint of 358 K, covering the full range of design feasibility from 318 K to 418 K.

It is immediately evident that the governing hypothesis of this study is positively validated. The simulation results show that coolant temperature had a significant effect on RCCI combustion characteristics. As shown in Figure 12b, the start of combustion occurred earlier with increasing wall temperatures, as the elevated thermal boundary conditions enhanced the temperature rise during the compression phase. Furthermore, combustion under elevated coolant temperatures resulted in a higher maximum CHR, which implied increased combustion efficiency, thus confirming the initial hypothesis.

The relevant effects are quantified in Figure 12b. A comparison of CA10 results shows that applying the highest available coolant temperature accelerated the initial combustion phase—associated with negative temperature coefficient (NTC) reactions and cool flames—from approximately −2.5 CAD (Cranke Angle Degree) at the baseline to −4.5 CAD.

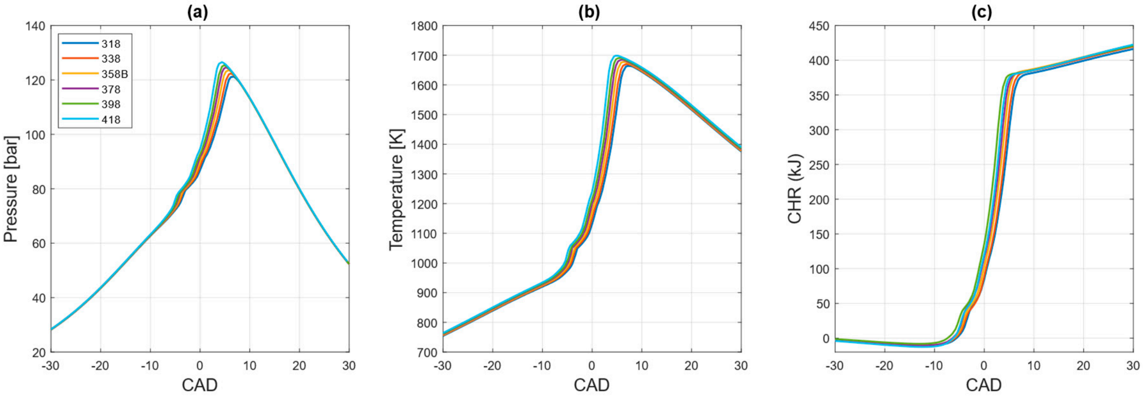

Figure 12. In-cylinder pressure, temperature, and cumulative heat release (CHR) at different coolant temperatures, swept around the baseline: Case B (25% load). (**a**) Pressure; (**b**) Temperature; (**c**) CHR.

The relevant effects are quantified in Figure 13. Comparing the CA10 results, one can note that applying the highest available coolant temperature accelerated the initial combustion phase (negative temperature coefficient reactions and cool flames) from approximately −2.5° CAD at baseline to −4.5° CAD. Note that, correspondingly, CA50 was reduced by the same 2° CAD, implying that the higher coolant temperature affected the start of combustion, while the combustion duration remained roughly the same. Ultimately, CA50 being phased closer towards TDC was the main reason for the increased peak pressure. The peak in-cylinder pressure increased by approx. 2 bar per 20 K of coolant temperature increase. Note that the trend here was almost fully linear (considering the modeling accuracy) despite the slight non-linearity of CA50, which was intertwined with the effect of combustion efficiency, as shown by the CHR plot in Figure 13c.

The sensitivity of combustion efficiency to coolant temperature was confirmed by trends in simulated CH_4. According to Figure 13, allowing the engine to be operated at the peak feasible coolant temperature, at low engine loads, provides prospects to cut down methane emissions by as much as 10% in comparison with the baseline case (358 K). Corresponding changes in CO emission were below the level of significance. While the model had not been re-calibrated for an exact match in absolute emission levels, the trends should be transferable to the experimental results. Note that emissions in RCCI are closely correlated to the thermal state of the mixture. On one end, the combined effects of lower heat losses, more rapid pressure rise rate, and combustion efficiency affected the bulk in-cylinder temperature, which increased from 1666 K at baseline to approx. 1674 K at the far-right side of the sweep. The sensitivity at the bulk level was not large, but higher temperature increments were observable in individual zones.

The above conclusions are indirectly supported by the corresponding gas-side component temperatures presented in Figure 14. The surface temperatures of key engine components exhibited a linear rise as the coolant temperature increased from 318 K to 418 K, indicating a direct correlation between coolant temperature and heat transfer within the engine.

The liner surface temperature (Figure 14a) increased from approximately 414 K to 489 K, representing a total rise of 75 K. Similarly, the cylinder head surface temperature (Figure 14b) rose from 428 K to 511 K, corresponding to a 19% increase over the tested coolant temperature range. These results suggest that as the coolant temperature increased, the rate of heat rejection to the cooling system decreased, leading to higher steady-state temperatures in the engine structures. While these elevated temperatures may have enhanced combustion efficiency, they also imposed greater thermal loads on engine materials.

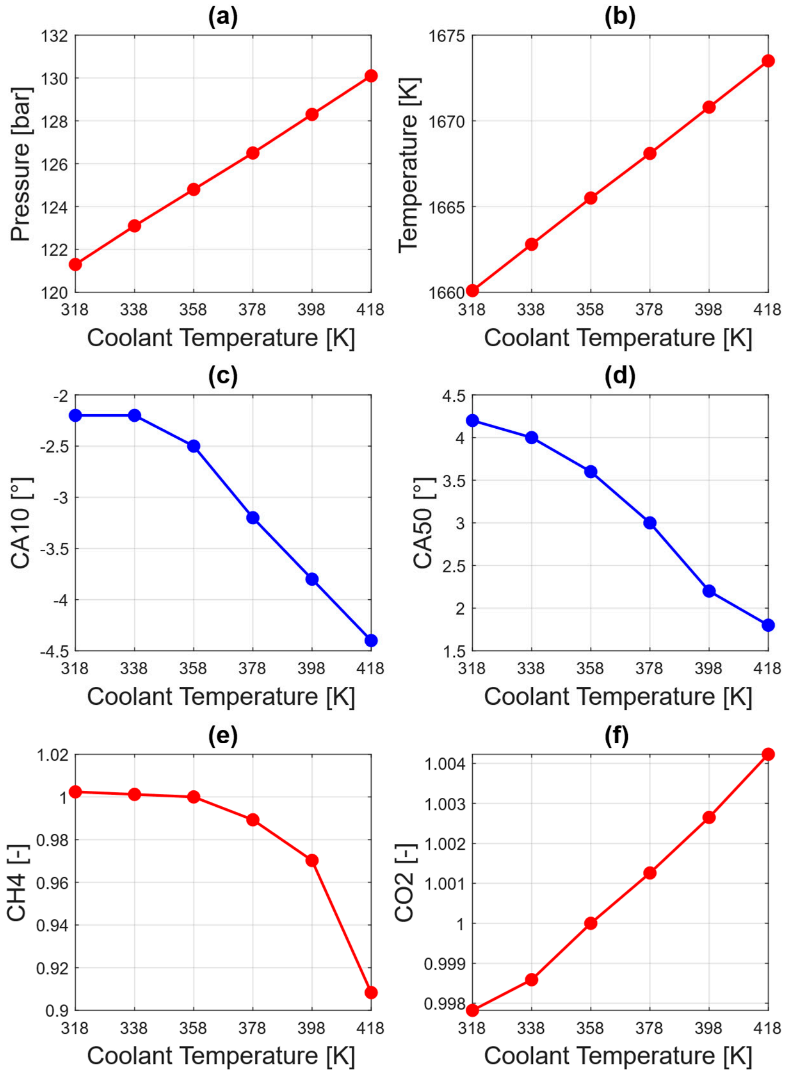

Figure 13. Relevant combustion indicators at different coolant temperatures: Case B (25% load). (**a**) Pressure; (**b**) Temperautre; (**c**) CA10; (**d**) CA50; (**e**) CH4; (**f**) CO_2.

Similarly, the exhaust valve face temperature (Figure 14c) exhibited a notable rise from 613 K to 668 K, equating to an increase of approximately 9%. However, the peak temperature remained roughly 68 K lower than the corresponding face-surface averaged exhaust valve temperature at peak engine load (refer to Figure 9), leaving a comfortable margin from the perspective of thermal stress.

The piston average surface temperature (Figure 14d) showed the smallest increase among all components, with the rise not exceeding 25 K across the entire coolant temperature sweep. This low sensitivity correlated with the minimal variation in the bulk cylinder gas temperature. This was expected, as the piston did not have direct access to the coolant, instead relying on crankcase oil as its primary cooling medium. The effect of the oil circuit is investigated in the following section.

Figure 15 links the discussion on component temperatures with their corresponding effects on combustion and emissions. More specifically, Figure 15 illustrates the impact of coolant and wall temperature on heat release rate, temperature evolution, and methane (CH_4) mass fraction across different cylinder gas zones. The zone numbers and locations corresponded to the UVATZ combustion model configuration presented in Figure 15.

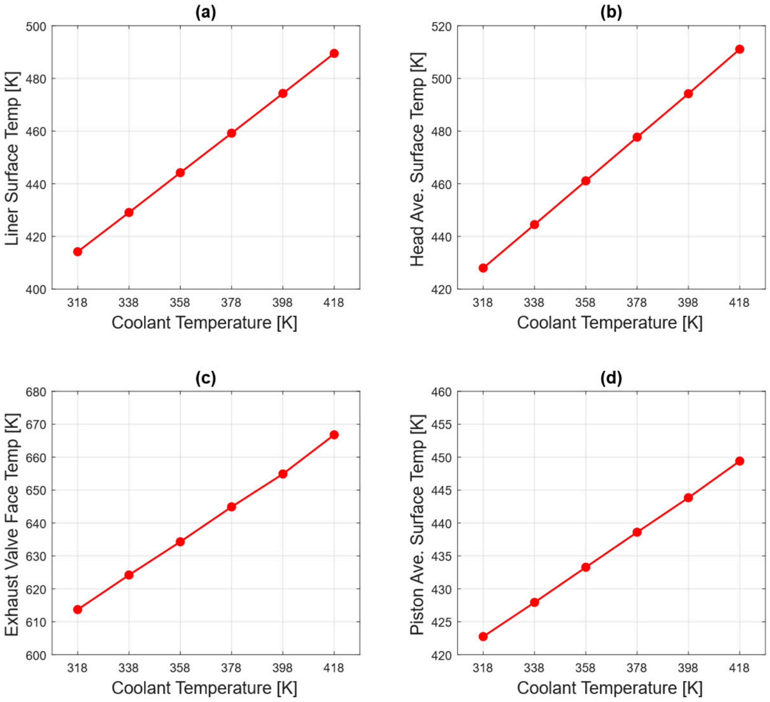

Figure 14. Effect of coolant temperature on key engine component surface temperatures: Case B (25% load). (**a**) Liner top side; (**b**) cylinder head; (**c**) exhaust valve face; and (**d**) piston.

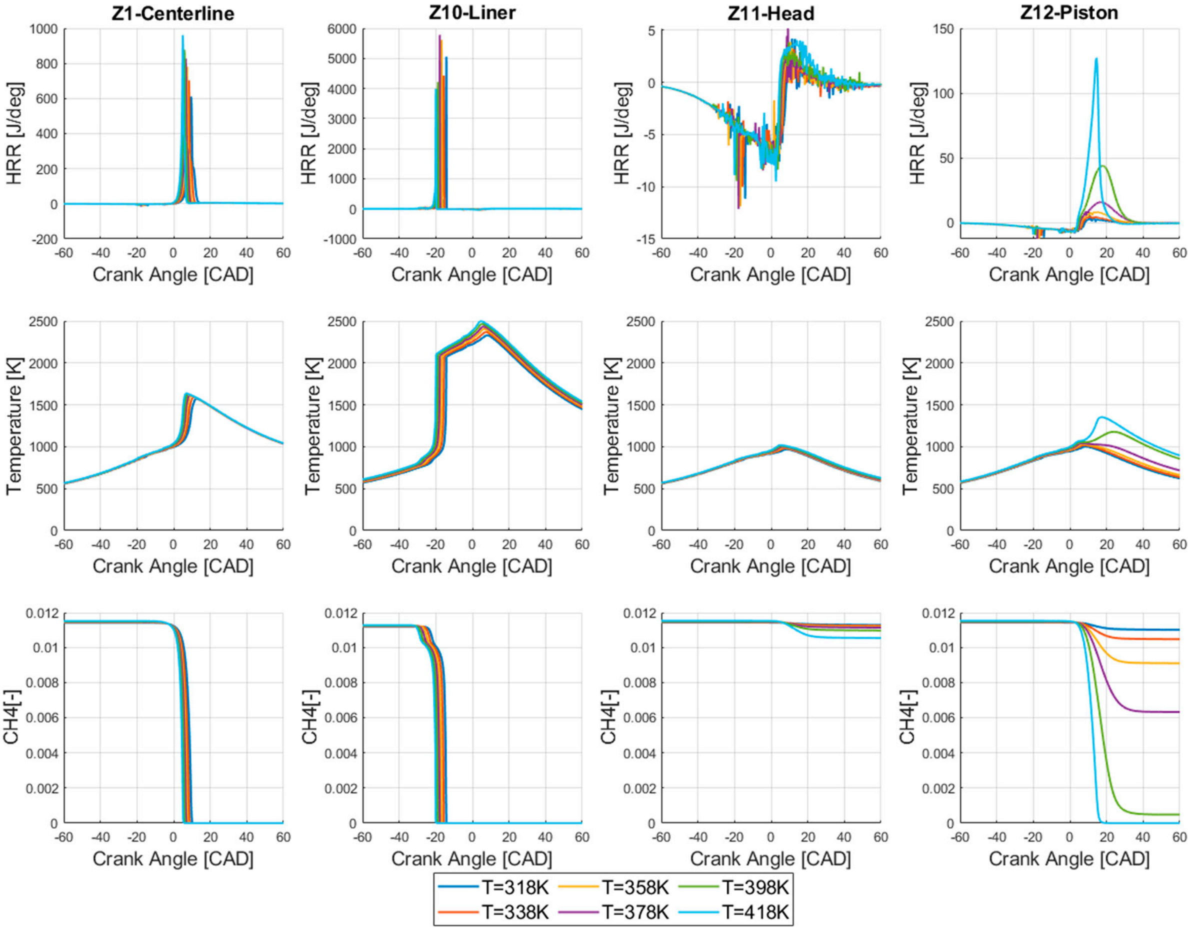

Figure 15. Effects of coolant temperature on heat release rate, temperature, and methane concentration in different cylinder zones: Case B (25% load). Baseline is T = 358 K.

It was observed that zone 10, adjoining the cylinder liner, exhibited high peak heat release rates, regardless of coolant temperature. This zone accumulated high concentrations of high-reactivity fuel because the early-injected diesel spray, after evaporation, was dispersed along the cylinder liner. Due to its high reactivity, this zone underwent nearly complete combustion, irrespective of the adjoining wall's thermal condition, as evidenced by the CH_4 mass fractions.

With reduced heat transfer from the gas to the wall, increased coolant temperature was found to affect the ignition timing in zone 10. Notably, negative temperature coefficient (NTC) reactions were initiated in this zone as early as −20 CAD aTDC (after top dead center), as evidenced by partial CH_4 consumption. The main exothermic reactions were observed to start between −15 CAD and −5 CAD aTDC, depending on the liner temperature. At that point, intensified heat and mass transfer of partially reformed species occurred from zone 10 toward zone 9 and onward, ultimately triggering the sequential combustion events propagating toward the cylinder centerline in zone 1 (Figure 15).

Combustion in zone 1 was found to be the least affected by wall temperature, which explained the relatively fixed offset between early combustion phasing (CA10) and later mass-burned instances (CA50). Reactivity-lean boundary zones 11 and 12, directly exposed to heat loss through adjoining head and piston surfaces, were observed to ignite last, consistent with their limited thermal energy and lower reactivity.

Figure 15 reveals that the reduction in methane slip under the low-load condition originated predominantly from more complete combustion occurring near the cylinder piston region, which remained the coldest area. Combustion in the piston region was minimal at the lowest coolant temperature, whereas at the highest coolant temperature, CH_4 conversion efficiency in this region reached approximately 99% in zone 12 compared with the piston boundary. Therefore, the reported ~10% reduction in CH_4 emissions for elevated coolant temperature in zone 11, the head, is attributed to the prevention of flame quenching near the cylinder head. To illustrate more insights into HRR, this specification is shown with different x-axis scales in the HRR row in Figure 15.

The remaining CH_4 emissions reported in Figure 15 originated from fractional contributions across all other reactive zones (zones 1–12), which, according to the simulation results, accounted for approximately 16% of the total methane slip at the highest coolant temperature. The other 84% was attributed to the crevice region and scavenging losses. It should be noted that the UVATZ model simplified both phenomena as a lumped contribution from a non-reactive crevice zone.

Although increasing coolant temperature was shown to improve low-load combustion efficiency and reduce methane slip, this strategy faces practical constraints under high-load operation. Elevated coolant temperatures can reduce knock and pre-ignition margins, increase component thermal loading—particularly for valves and the cylinder head—and limit the allowable pressure rise rate. As a result, any coolant-temperature elevation must be restricted to low-load regions and carefully integrated with ECU thermal and combustion safety boundaries. These limitations highlight the need for load-dependent thermal management rather than a uniform coolant-temperature increase [29].

7.2. Effect of Crankcase Oil Temperature

In the oil boundary conditions outlined in Table 3, two distinct temperature boundaries were considered: piston oil temperature and cylinder oil temperature. This study analyzed the piston oil temperature sweep, as it depended solely on crankcase oil cooling. This provided an opportunity to decouple the influence on combustion from other thermal phenomena, which were discussed more comprehensively in the preceding subsection.

Figure 16 illustrates how the temperature of the oil in the crankcase, in a range of 313 K to 373 K, affects in-cylinder pressure, temperature and CHR over the combustion cycle. It should be noted that the case denoted as 333 K represents the reference, Case B, which was also included in the coolant sweep. Comparison of the results in Figure 16 with those in Figure 12 reveals that oil temperature variation had a much smaller effect on combustion characteristics than the corresponding variation in coolant temperature.

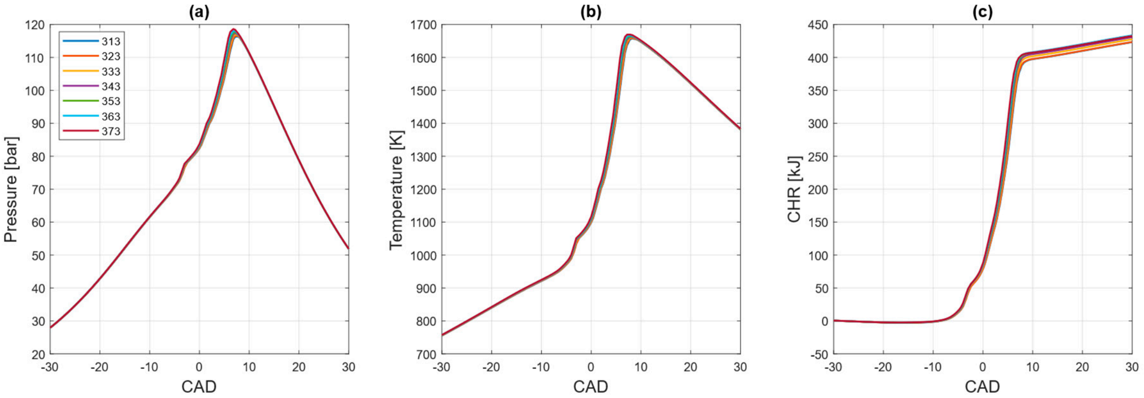

Figure 16. In-cylinder pressure, temperature, and cumulative heat release (CHR) at different lube oil temperatures, swept around the baseline: Case B (25% load). (**a**) Pressure; (**b**) Temperature; (**c**) CHR.

Figure 17 presents the quantified effects of oil temperature on in-cylinder thermodynamic properties. In short, the start of combustion remained almost uninfected, as the changes in CA10 were irrelevant from the perspective of model accuracy (±0.5 CAD). The trend was, however, consistent and magnified while the combustion approached 50% of mass burned. More explicitly, CA50 consistently decreased with piston oil temperature, implying reduced combustion duration. This corresponded to reduced CH4 emissions, but the improvement potential is roughly half of that imposed by the coolant temperature. In line with the above trends were the effects on peak pressure and temperature, influenced by combustion phasing and reduced heat loss, as discussed in the previous section.

Collectively, these plots demonstrate that increasing oil temperature enhanced combustion efficiency, accelerated combustion timing, and reduced unburned fuel—all key indicators of improved engine thermal behavior. Subplots e and f show the trends of normalized CH_4 and CO_2 mass fractions. As the oil temperature rose, the CH_4 mass fraction (subplot e) decreased from approximately 1.01 to 0.96, equating to a reduction of about 1.4%. Meanwhile, the CO_2 mass fraction (subplot f) increased slightly, from approximately 0.9995 to 1.0018, indicating the low sensitivity of CO_2 emissions to oil temperature overall.

The small magnitude of changes invoked by oil temperature alterations finds explanation in the component temperature changes illustrated in Figure 18. It is immediately evident that there was no significant effect on the surface temperature of the head or valve components, as these parts remained isolated from the crankcase oil cooling circuit. In both cases, the variation in surface temperature did not exceed 3 K across the entire sweep range, and the observed effects were solely attributed to increased bulk cylinder gas temperatures (refer to Figure 18b). The piston exhibited the highest sensitivity, with its surface temperature increasing approximately 1:1 with the rise in oil temperature. Since the lower parts of the liner were exposed to the crankcase region, the combustion chamber surface of the liner experienced reduced heat transfer through the structure as oil temperature increased.

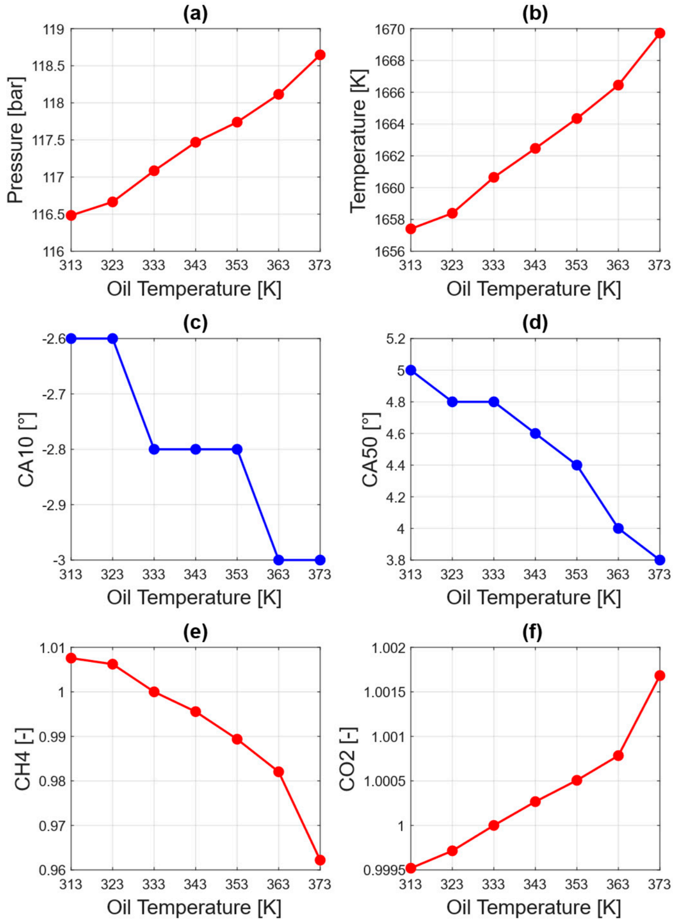

Figure 17. Relevant combustion indicators at different crankcase oil temperatures: Case B (25% load). (**a**) Pressure; (**b**) Temperature; (**c**) CA10; (**d**) CA50; (**e**) CH4; (**f**) CO_2.

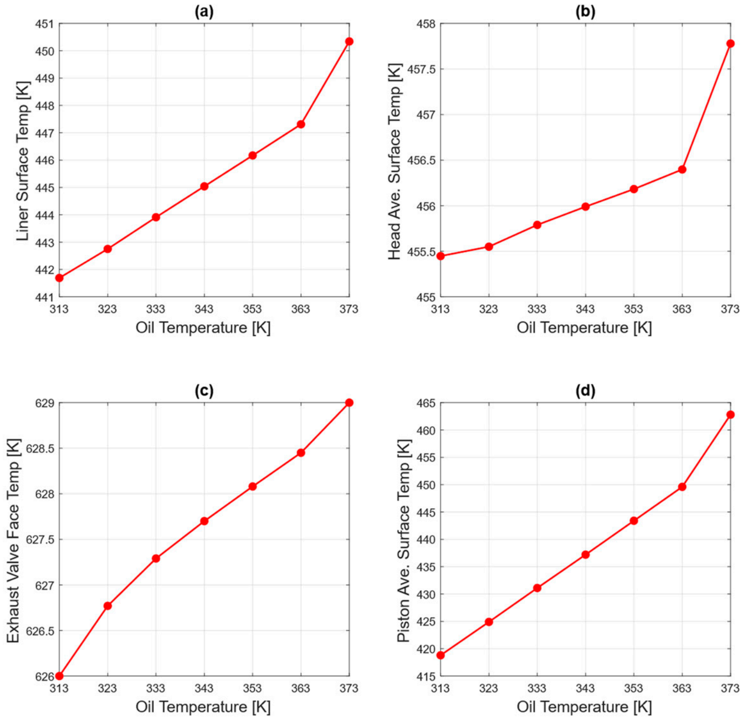

Figure 18. Effect of crankcase oil temperature on engine component surface temperatures: (**a**) liner; (**b**) cylinder head; (**c**) exhaust valve face; and (**d**) piston—Case B (25% load).

Analysis of Figure 16, in the context of Figure 19, further explains the impact of cylinder component temperatures on combustion and emissions, as discussed earlier. Zone 11, located adjacent to the cylinder head, was identified as the largest contributor to unburned hydrocarbons. Therefore, adjusting oil temperature had only a minor effect on overall improvements in combustion efficiency. On the other hand, zone 12, as the piston boundary condition, exhibited more sensitivity to oil temperature change, as depicted in Figure 19.

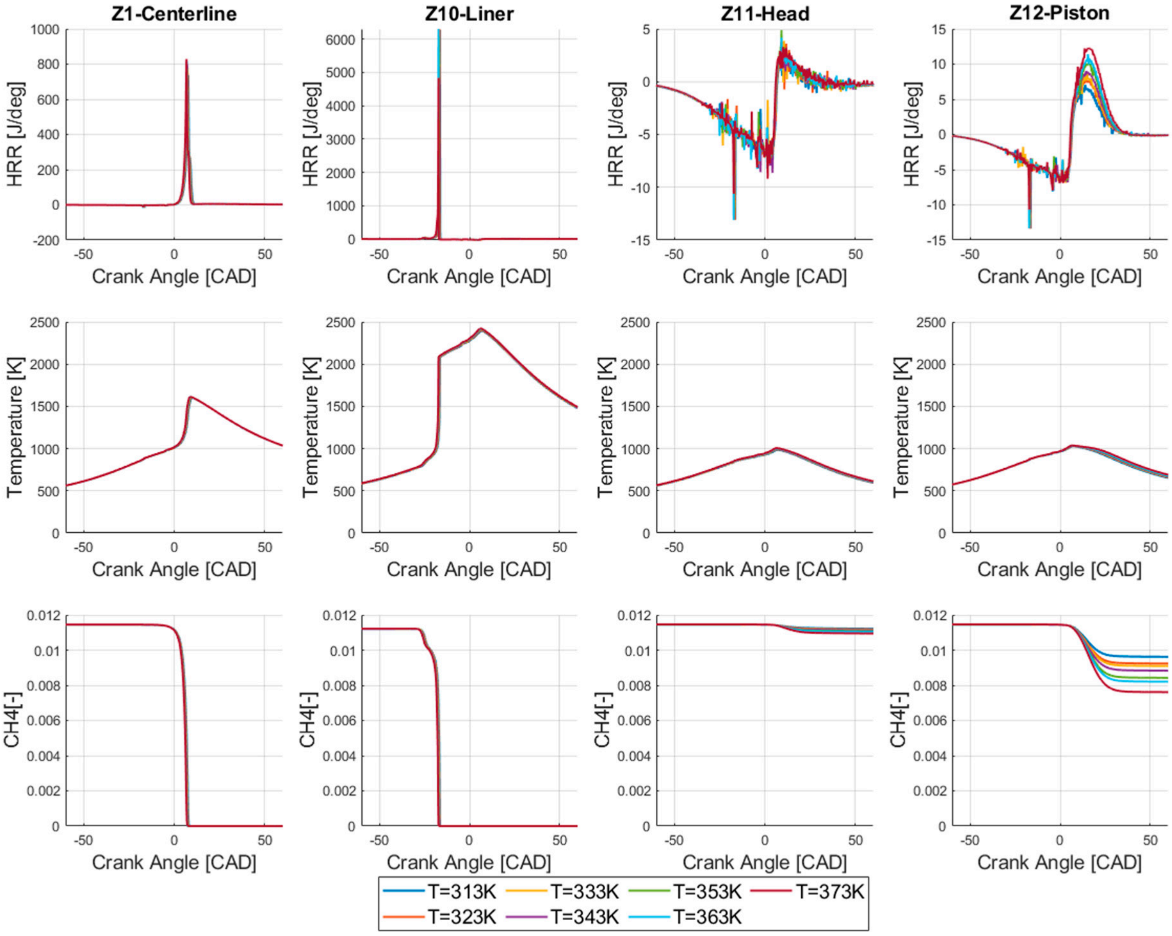

Figure 19. Effects of oil temperature as coolant on heat release rate, temperature, and methane concentration in different zones simulated by UVATZ code: Case B. Baseline is T = 313 K.

Figure 19 shows the impact of oil temperature—acting as a coolant—on HRR, temperature evolution, and methane (CH_4) concentration in various zones simulated by the UVATZ code. The Z10–liner zone exhibits the highest HRR and peak temperatures due to its proximity to the combustion chamber walls, with only minor shifts in combustion phasing observed as oil temperature increased.

Higher oil temperatures resulted in reduced heat loss, which led to slightly elevated in-cylinder temperatures and a marginal delay in CH_4 oxidation, particularly in the Z11–head region. While the HRR remained mostly unchanged, the lower heat dissipation caused a subtle shift in combustion phasing and delayed methane oxidation. These effects could influence both combustion efficiency and NO_x emissions under certain operating conditions.

In summary, the results indicate that oil temperature alone did not drastically alter combustion characteristics. Nevertheless, optimized oil temperature management was shown to contribute to reducing frictional losses, improving fuel utilization, and enhancing engine longevity. However, excessively high oil temperatures could have compromised lubrication performance and increased thermal stress on engine components.

More broadly, adjusting coolant and oil temperatures as a strategy for reducing methane slip in RCCI combustion was shown to involve trade-offs with NO_x emissions. Although NO_x was not explicitly simulated in this study, experimental RCCI results used as a baseline for simulation confirmed that NO_x levels remained ultra-low, staying well below the stringent Euro 6 automotive limits.

This fact, along with the wide thermal and mechanical stress margins observed in the study, supports the viability of coolant-based thermal management as an effective strategy to partially mitigate low combustion efficiency issues during low-load operation in next-generation marine dual-fuel (DF) engines.

7.3. Reducing Thermal Loading at High Engine Loads with RCCI Combustion Control

Figure 20 shows coolant temperature results and indicates that elevating the coolant temperature could significantly reduce methane slip, one of the governing challenges of RCCI at low engine loads. On the other hand, Section 3.2 already implies that with the baseline setpoints for the cooling circuit temperatures, RCCI operated on the edge of permittable component thermal loading during high-load RCCI operation. Focusing on this high-load regime, this section aims to provide an understanding of how combustion control could limit the thermal loading of RCCI, thus creating a higher margin for coolant circuit-based thermal management, addressing Objective 4b, as set out earlier. Referring to Table 4, a combined lambda and blend ratio sweep (Campaign 4), around the baseline 83% load point (Case F), was selected for this purpose.

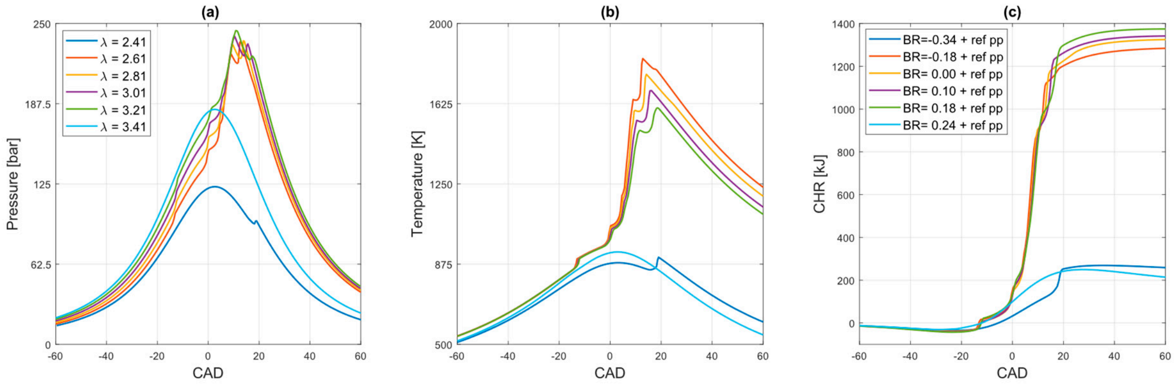

Figure 20. Effects of varying lambda values (2.41 to 3.41) on key combustion parameters—(**a**) in-cylinder pressure; (**b**) temperature; (**c**) cumulative heat release (CHR)—as functions of crank angle (CAD). λ = 2.61 indicates the baseline, Case B.

In-cylinder pressure (Figure 20a), temperature (Figure 20b), and cumulative heat release (Figure 20c) are shown as functions of crank angle degree (CAD) for various points in the sweep, denoted by lambda (λ) and blend ratio (BR) increments relative to the reference case.

At first glance, it was observed that there was a relatively narrow window for controlling the combustion process, constrained by misfire near the upper and lower flammability limits. More explicitly, when λ was reduced by more than -0.2 from the reference case, the mixture failed to ignite completely, as evidenced by significantly lower peak pressure, temperature, and CHR values.

In the investigated case, λ was controlled by adjusting the boost pressure while keeping the total fuel energy input constant. Lowering the boost pressure, and consequently, the trapped in-cylinder charge at IVC, resulted in insufficient compression temperatures to ignite the diesel pilot fuel well before TDC. Consequently, the natural gas-lean regions were ignited very late—approximately 18 CAD aTDC—after being penetrated by partial combustion products from diesel auto-ignition. At that point, the combustion process was hindered by the ongoing cylinder expansion.

In principle, stable combustion could still be obtained at the given λ setpoint by further reducing the natural gas–diesel BR. However, this was not considered economically or environmentally viable from an application standpoint. Furthermore, from a simulation perspective, such a condition would violate the governing assumption of fully reactivity-controlled combustion, thereby rendering the current combustion model incapable of reproducing valid trends.

Misfire occurred at the upper end of the lambda (λ) sweep when the mixture exceeded the upper flammability limit of the gaseous fuel, corresponding to λ + 0.8 from the reference case. As observed in the CHR plot (Figure 16), the portion of the mixture sufficiently seeded by diesel—specifically in zones near the cylinder liner—underwent combustion, but ignition failed to propagate into the reactivity-lean regions of the cylinder. Consequently, increasing the diesel ratio slightly extended the zones penetrated by the diesel spray, yet this did not prevent partial misfire from occurring.

Considering the feasible lambda (λ)–blend ratio (BR) operating range, the temperature trend plotted in Figure 20 substantiates the combustion-based thermal management strategy. Increasing mixture dilution by elevating λ allowed for a significant reduction in combustion temperature throughout the entire cycle, while maintaining the same overall energy input.

In the absence of direct COV and ringing-intensity outputs in the 1D–MZM framework, λ/BR stability was evaluated using established surrogate indicators such as PRR limits, phasing sensitivity, and convergence stability, which correlate well with conventional combustion-stability criteria reported in the RCCI literature [12].

At high load, variations in λ and blend ratio significantly modify the in-cylinder thermal field, which in turn affects several ECU calibration constraints. As seen in Figure 20, richer mixtures and higher reactivity blends elevate peak pressure and temperature gradients, pushing the pressure rise rate (PRR) closer to calibration limits and reducing the available safety margin for knock and pre-ignition control. The increased thermal severity near top dead center also heightens the sensitivity of auto-ignition behavior, requiring more conservative start-of-energizing (SOE) phasing to avoid premature combustion onset. Conversely, operating at a higher λ reduces peak temperatures by nearly 200 K, lowering both PRR and knock likelihood but potentially delaying heat release and demanding compensatory SOE adjustments. These interactions highlight that any λ–blend ratio strategy aimed at thermal-load mitigation must be evaluated jointly with ECU boundaries to ensure robust high-load operability without exceeding PRR, knock, or SOE constraints.

It should be noted that mixture strength had a substantial impact on mixture reactivity and thus on combustion phasing in RCCI mode. To address this, simultaneous adjustment of BR was successfully applied to maintain combustion phasing near a consistent setpoint. This effect can be clearly observed in 20c. This enabled the evaluation of thermal management potential through λ control under the relevant assumption of optimal indicated efficiency. It is also evident in Figure 20a that the adopted strategy kept peak cylinder pressure well below the 250-bar mechanical durability limit. Importantly, the observed reduction in in-cylinder temperatures was achieved without compromising power output. The gross CHR curves saturated at higher levels, primarily due to reduced heat loss to the cylinder walls.

Figure 21 enables quantification of the above observations. One can clearly observe that the adopted strategy was able to cut the bulk in-cylinder temperature by approximately 200 K, to a level similar to the low-load case. At the same time, CA50 was kept within

+/−1.5 CAD of the reference point. The difference is comparable with cycle-to-cycle variations typically observed in RCCI and so remains negligible from the perspective of both modeling accuracy and impact on efficiency. The CH_4 concentrations reduced drastically, but this was predominantly caused by the higher mixture dilution. Interestingly, however, operating at leaner mixtures supported more complete combustion, with a reduction in CH_4 mass of around 15%. The baseline CH_4 emission level in high-load RCCI was already small, so the reduction was an order of magnitude smaller than at low-load operation. Note that a lower lambda should further provide lower NO_x emissions by reducing the intensity of the thermally driven Zeldovich mechanism. This could not be concluded directly from the results, but the effect is well known from the literature [79,82].

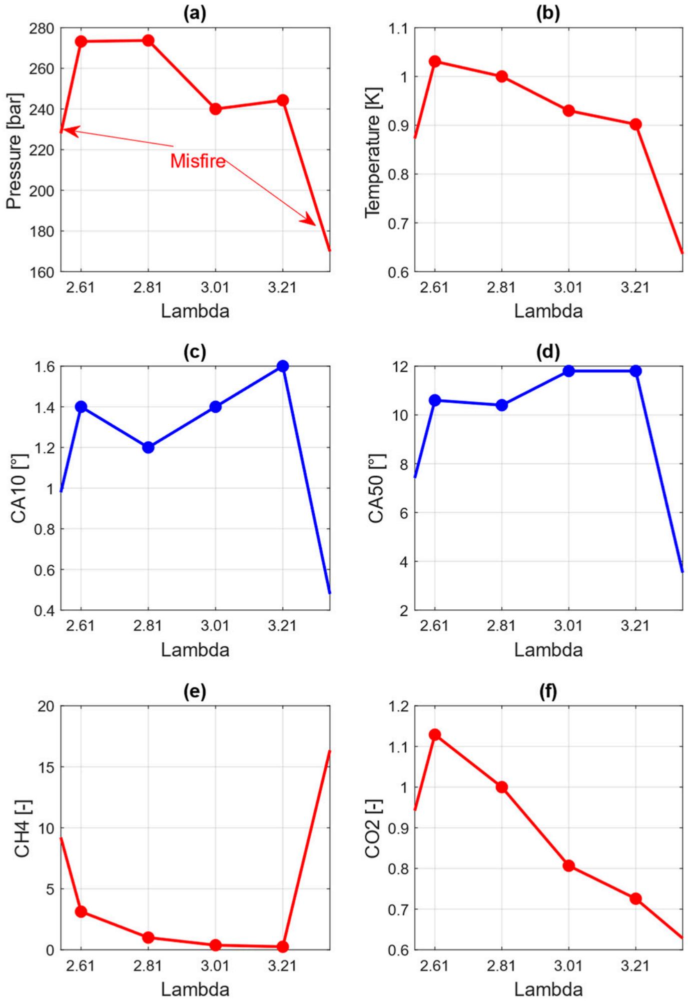

Figure 21. Impact of lambda variations (2.41 to 3.41) on combustion and emissions characteristics, showing trends for (**a**) peak pressure; (**b**) peak temperature; (**c**) combustion phasing (CA10); (**d**) combustion phasing (CA50); (**e**) CH_4 emissions; and (**f**) CO_2 emissions: Case F.

The prospect of lowering thermal stress while maintaining improved performance is regarded as the main premise for lambda control in RCCI. Figure 22 substantiates this, showing the changes in surface temperatures of relevant engine components under different lambda conditions. Abstracting from the misfire cases, a consistent drop in temperatures for all components was noted as the cylinder mixture became more diluted. The exhaust valves were subjected to the highest thermal stress, with their baseline face-averaged temperature recorded at 742 K. When lambda was elevated to the boundary of stable combustion, the component temperature was reduced by as much as 35 K. At the same time, the local hot-spot temperature of the valve surface decreased from 789 K to 736 K. This reduction lowers the risk of both thermal durability issues and hot-spot pre-ignition, thereby allowing hydrogen-enriched RCCI to be enabled without derating.

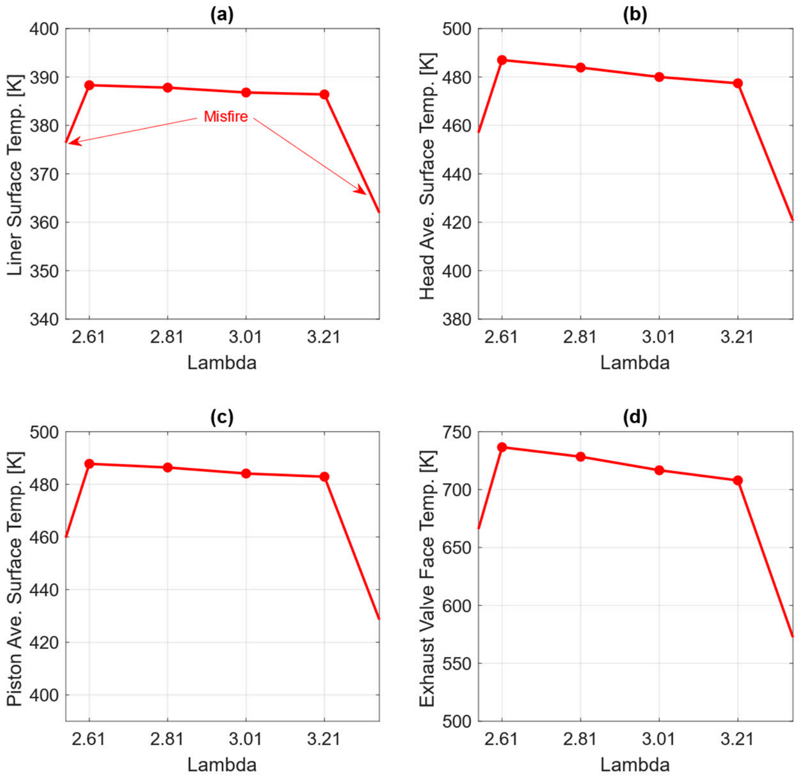

Figure 22. Variation in key engine component surface temperatures as a function of lambda: (**a**) the liner; (**b**) head average; (**c**) piston average; and (**d**) exhaust valve face: Case F.

The reductions in other component temperatures were much smaller, as these components were exposed to hot exhaust gases for a shorter duration. The head, on a surface-averaged basis, was cooled from 487 K at baseline to 476 K under lean conditions. The piston experienced a similar reduction of roughly 10 K. At this point, it should be noted that the component temperature reductions shown in Figure 22 are an order of magnitude lower than the reduction in bulk cylinder temperature shown in Figure 20. This was understood when taking into context the results discussed earlier Section 7.3. Firstly, based on Figure 22, it was established that excessive thermal loading during high-load RCCI operation was predominantly caused by excessive peak in-cylinder pressures, which significantly increased the heat transfer rates in the boundary zones. These heat transfer rates were found to remain largely unaffected by lambda. Secondly, it was shown that in-cylinder temperature had only a secondary impact and that increasing lambda elevated only the combustion/exhaust temperatures. As evidenced in Figure 22, in-cylinder temperatures remained unchanged during the remaining half of the cycle (intake and compression).

The main takeaway of this section is considered to be of applied significance. It was shown that the temperatures of components such as exhaust valves and valve seats subjected to excessive thermal loading in RCCI could be meaningfully reduced by adjusting the mixture strength. This was achieved without overcooling the CH_4/CO formation-sensitive regions of the cylinder, thereby maintaining the benefits of ultra-low emissions. At the same time, the single percentage point elevation of the natural gas–diesel blend ratio, which was necessary to retain optimum phasing, was found not to have a significant negative impact on CO_2 emissions. The elevated blend ratio was further regarded as advantageous from the perspective of fuel-flexible operation in hydrogen-enriched RCCI mode. Importantly, the amount of feasible H_2 admixtures in RCCI was increased by wider margins of blend ratio control (as limited by diesel injector ballistic operation), and hot-spot temperatures were reduced, thereby preventing pre-ignition.

8. Conclusions and Outlook

This study developed and validated an integrated RCCI–thermal co-simulation framework capable of rapidly predicting the interaction between reactivity-controlled combustion and component heat loading. The coupled UVATZ–GT-Power–FEA approach demonstrated strong agreement with the experimental data, confirming its predictive capability for both combustion behavior and component temperatures while maintaining runtimes suitable for system-level development.

- The results revealed that RCCI operation induces large temperature differences across load ranges, creating challenges for both combustion stability at low load and thermal stress at high load. Low-load analysis showed that overcooling of cylinder head regions, rather than the liner, is a dominant contributor to methane slip and flame quenching. Conversely, high-load conditions produced substantial heat transfer and severe exhaust-valve temperatures, identifying hot-spot-induced pre-ignition as a key constraint for future RCCI fuel-flexibility strategies.

The sensitivity study demonstrated that modest increases in component temperatures can improve low-load combustion and reduce methane slip, while coordinated λ–blend ratio adjustments at high load can reduce peak combustion temperatures and mitigate pre-ignition risks without compromising performance. These findings highlight the importance of integrated thermal combustion calibration for RCCI engines.

Finally, although the framework provides reliable predictions of thermal behavior and combustion performance, the emissions results remain limited by the absence of a NO_x submodel and simplified CO/HC chemistry. Future work will extend the UVATZ mechanism to include detailed NO_x and oxidation pathways to enhance emission predictiveness across the full load range.

Outlook

The conclusions above highlight the wide applicability of the new framework toward the development of next-generation marine engines. At the same time, this research has identified two limitations on the modeling assumptions that constrain the scope and accuracy of the present study.

First, the predictivity in emissions was limited by the shortcomings of the mechanism used and the coarse nature of the imposed zonal configuration. The n-heptane–natural gas mechanism of Yao et al. [6] was selected for its stability, fast simulation time, and accuracy in predicting performance parameters. The model did not include the NO_x formation pathway, which limited the study's insight into CO/CH_4 formation. The issue has already been comprehensively handled in the CASEMATE project [30], where a novel mechanism for robust simulation of multi-component fuel blends has been developed and coupled with UVATZ combustion, followed by successful validation in engine conditions [5]. Aside from securing predictivity in NO_x, the mechanism considered improved kinetics of ammonia and H_2 in cross-interactions with existing n-heptane–natural gas pathways.

The second limitation was that the current zonal configuration of the UVATZ model (Figure 2) did not fully exploit the capabilities of the detailed thermal solver. From the perspective of combustion codes, the influence of wall temperature is captured on a lumped basis, considering streams coming from the cylinder head, liner, and piston. More detailed discretization of these gas-side boundary zones around the liner head region and crevice would further increase the model's emissions predictivity, reproducing relevant phenomena related to hot-source pre-ignition. The combustion zone generation could become automatic, based on the detailed geometrical parametrization available from the FEM-based thermal solver. This functionality would improve the thermal combustion interface. It would also open geometry-enhanced features for improving UVATZ physics-based sub-models: squish-region-invoked turbulence and physical spray-wall interaction. This development is part of the current Flex-CPT project [84].

The new framework provides a unique combination of extensive insight and rapid simulation time, making it suitable for various model-based development applications in the LTC engine domain. The simulation time remained limited by the UVATZ combustion code, taking around 70% of the computational effort, with the thermal solver being the least computationally expensive. The recent activities in CASEMATE [81] have shown that the UVATZ solution can be optimized, cutting the closed-cycle simulation time from around 180 s (the version used in this study) to less than 35 s. Acceleration potential increases exponentially with increased zonal resolution. This is believed to be achievable without loss in accuracy, primarily by decoupling the flow and kinetic solutions in each zone so that they can be solved in parallel instead of sequentially. The follow-up activities anticipate using the accelerated UVATZ solver, coupled with an improved thermal framework, to support large-scale DOE runs in a multi-cylinder engine, or for system-level simulation, drastically increasing its applicability potential.

Author Contributions: Conceptualization, A.K., J.H. and M.M.; Methodology, A.K. and M.M.; Software, A.K., K.G., A.V. and B.S.; Validation, A.K., K.G., A.C., A.V. and B.S.; Formal analysis, A.K.; Investigation, A.K., K.G. and S.M.; Writing—original draft, A.K., K.G., S.M. and M.M.; Writing—review & editing, A.K.; Visualization, A.K., A.C., A.V., S.M., A.M.A., B.S., J.H. and M.M.; Supervision, A.M.A., J.H. and M.M. All authors have read and agreed to the published version of the manuscript.

Funding: The results were achieved in the CASEMATE project (ref. 2919/31/2022) that was co-funded by Business Finland.

Data Availability Statement: The original contributions presented in the study are included in the article, further inquiries can be directed to the corresponding author.

Conflicts of Interest: The authors declare no conflict of interest.

Abbreviations

Abbreviation	Full Term
A/F ratio	air-to-fuel ratio
aTDC	after top dead center
bTDC	before top dead center
BR	blend ratio
CA10/CA50	crank angle at 10%/50% mass burned
CAD	crank angle degree
CFD	computational fluid dynamics
CH_4	methane
CHR	cumulative heat release
CO	carbon monoxide
CO_2	carbon dioxide
DF	dual-fuel
ECU	engine control unit
EVO	exhaust valve opening
FEM	finite element method
GT-Suite	Gamma Technologies Simulation Suite
H_2	hydrogen

HCCI	homogeneous charge compression ignition
HRF	high-reactivity fuel
HTC	heat transfer coefficient
IMEP	indicated mean effective pressure
ISAC	indicated specific air consumption
ISFC	indicated specific fuel consumption
ITE	indicated thermal efficiency
IVC	intake valve closing
LRF	low-reactivity fuel
LTC	low-temperature combustion
MZM	multi-zone model
NG	natural gas
RCCI	reactivity-controlled compression ignition
SOE	start of energizing
TDC	top dead center
TPA	three pressure analysis
TR	trapping ratio
UVATZ	University of Vaasa Advanced Thermo-kinetic multi-Zone
VE	volumetric efficiency
λ	lambda (air–fuel equivalence ratio)

References

1. Ahmad, Z.; Kaario, O.; Qiang, C.; Vuorinen, V.; Larmi, M. A parametric investigation of diesel/methane dual-fuel combustion progression/stages in a heavy-duty optical engine. *Appl. Energy* **2019**, *251*, 113191. [CrossRef]
2. Kahila, H.; Wehrfritz, A.; Kaario, O.; Vuorinen, V. Large-eddy simulation of dual-fuel ignition: Diesel spray injection into a lean methane-air mixture. *Combust. Flame* **2019**, *199*, 131–151. [CrossRef]
3. Mikulski, M.; Balakrishnan, P.R.; Hunicz, J. Natural gas-diesel reactivity controlled compression ignition with negative valve overlap and in-cylinder fuel reforming. *Appl. Energy* **2019**, *254*, 113638. [CrossRef]
4. Li, J.; Yang, W.; Zhou, D. Review on the management of RCCI engines. *Renew. Sustain. Energy Rev.* **2017**, *69*, 65–79. [CrossRef]
5. Kakoee, A.; Gharehghani, A. Comparative study of hydrogen addition effects on the natural-gas/diesel and natural-gas/dimethyl-ether reactivity controlled compression ignition mode of operation. *Energy Convers. Manag.* **2019**, *196*, 92–104. [CrossRef]
6. Gharehghani, A.; Kakoee, A.; Andwari, A.M.; Megaritis, T.; Pesyridis, A. Numerical investigation of an RCCI engine fueled with natural gas/dimethyl-ether in various injection strategies. *Energies* **2021**, *14*, 1638. [CrossRef]
7. Benajes, J.; Pastor, J.V.; García, A.; Monsalve-Serrano, J. The potential of RCCI concept to meet EURO VI NO_x limitation and ultra-low soot emissions in a heavy-duty engine over the whole engine map. *Fuel* **2015**, *159*, 952–961. [CrossRef]
8. García Valladolid, P.; Tunestål, P.; Monsalve-Serrano, J.; García, A.; Hyvönen, J. Impact of diesel pilot distribution on the ignition process of a dual fuel medium speed marine engine. *Energy Convers. Manag.* **2017**, *149*, 192–205. [CrossRef]
9. Xia, L.; Willems, R.; de Jager, B.; Willems, F. Constrained Optimization of Fuel Efficiency for RCCI Engines. *IFAC-PapersOnLine* **2019**, *52*, 648–653. [CrossRef]
10. Ansari, E.; Shahbakhti, M.; Naber, J. Optimization of performance and operational cost for a dual mode diesel-natural gas RCCI and diesel combustion engine. *Appl. Energy* **2018**, *231*, 549–561. [CrossRef]
11. Paykani, A.; Garcia, A.; Shahbakhti, M.; Rahnama, P.; Reitz, R.D. Reactivity controlled compression ignition engine: Pathways towards commercial viability. *Appl. Energy* **2021**, *282*, 116174. [CrossRef]
12. Paykani, A.; Kakaee, A.-H.; Rahnama, P.; Reitz, R.D. Progress and recent trends in reactivity-controlled compression ignition engines. *Int. J. Engine Res.* **2016**, *17*, 481–524. [CrossRef]
13. Kokjohn, S.L.; Hanson, R.M.; Splitter, D.A.; Reitz, R.D. Fuel reactivity controlled compression ignition (RCCI): A pathway to controlled high-efficiency clean combustion. *Int. J. Engine Res.* **2011**, *12*, 209–226. [CrossRef]
14. Mikulski, M.; Bekdemir, C. Understanding the role of low reactivity fuel stratification in a dual fuel RCCI engine—A simulation study. *Appl. Energy* **2017**, *191*, 689–708. [CrossRef]
15. Wang, S.; Chong, C.T.; Józsa, V.; Chiong, M.-C. Investigation of NO emissions and chemical reaction kinetics of ammonia/methane flames under dual-fuel co-combustion mode at elevated air temperature conditions. *Int. J. Hydrogen Energy* **2024**, *84*, 968–981. [CrossRef]
16. Park, K.H. Effect of cylinder wall temperature on marine engine combustion. *JAMET* **2023**, *47*, 309–316. [CrossRef]

17. Vasudev, A.; Mikulski, M.; Balakrishnan, P.R.; Storm, X.; Hunicz, J. Thermo-kinetic multi-zone modelling of low temperature combustion engines. *Prog. Energy Combust. Sci.* **2022**, *91*, 100998. [CrossRef]
18. Lashkarpour, S.M.; Khoshbakhti Saray, R.; Najafi, M. Multi-zone model for reactivity controlled compression ignition engine based on CFD approach. *Energy* **2018**, *156*, 213–228. [CrossRef]
19. Komninos, N.P.; Rakopoulos, C.D. Heat transfer in hcci phenomenological simulation models: A review. *Appl. Energy* **2016**, *181*, 179–209. [CrossRef]
20. Ekberg, K.; Leek, V.; Eriksson, L. Validation of an Open-Source Mean-Value Heavy-Duty Diesel Engine Model. In Proceedings of the 59th Conference on Simulation and Modelling (SIMS 59), Oslo, Norway, 26–28 September 2018; pp. 290–296. [CrossRef]
21. Hautala, S.; Mikulski, M.; Söderäng, E.; Storm, X.; Niemi, S. Toward a digital twin of a mid-speed marine engine: From detailed 1D engine model to real-time implementation on a target platform. *Int. J. Engine Res.* **2022**, *24*, 4553–4571. [CrossRef]
22. Stoumpos, S.; Theotokatos, G.; Mavrelos, C.; Boulougouris, E. Towards Marine Dual Fuel Engines Digital Twins—Integrated Modelling of Thermodynamic Processes and Control System Functions. *J. Mar. Sci. Eng.* **2020**, *8*, 200. [CrossRef]
23. Sixel, E.J.; Hiltner, J.; Rickert, C. Use of 1-D simulation tools with a physical combustion model for the development of Diesel-Gas or Dual Fuel engines. In Proceedings of the 28th CIMAC World Congress on Combustion Engine Technology, Helsinki, Finland, 6–10 June 2016; pp. 6–10.
24. Bekdemir, C.; Baert, R.; Willems, F.; Somers, B. *Towards Control-Oriented Modeling of Natural Gas-Diesel RCCI Combustion*; SAE International: Warrendale, PA, USA, 2015. [CrossRef]
25. Hultqvist, A.; Engdar, U.; Johansson, B.; Klingmann, J. *Reacting Boundary Layers in a Homogeneous Charge Compression Ignition (HCCI) Engine*; SAE International: Warrendale, PA, USA, 2001. [CrossRef]
26. Kakoee, A.; Vasudev, A.; Smulter, B.; Hyvonen, J.; Mikulski, M. *A Predictive 1D Modeling Framework for Reactivity-Controlled Compression Ignition Engines, via a Chemistry-Based, Multizone Combustion Object*; SAE International: Warrendale, PA, USA, 2023. [CrossRef]
27. Kokjohn, S.L.; Musculus, M.P.B.; Reitz, R.D. Evaluating temperature and fuel stratification for heat-release rate control in a reactivity-controlled compression-ignition engine using optical diagnostics and chemical kinetics modeling. *Combust. Flame* **2015**, *162*, 2729–2742. [CrossRef]
28. Jia, M.; Gingrich, E.; Wang, H.; Li, Y.; Ghandhi, J.B.; Reitz, R.D. Effect of combustion regime on in-cylinder heat transfer in internal combustion engines. *Int. J. Engine Res.* **2016**, *17*, 331–346. [CrossRef]
29. Someya, S.; Okura, Y.; Munakata, T.; Okamoto, K. Instantaneous 2D imaging of temperature in an engine cylinder with flame combustion. *Int. J. Heat Mass Transf.* **2013**, *62*, 382–390. [CrossRef]
30. Zhao, P.; Wang, L.; Chakraborty, N. Effects of the cold wall boundary on the flame structure and flame speed in premixed turbulent combustion. *Proc. Combust. Inst.* **2021**, *38*, 2967–2976. [CrossRef]
31. Zhao, P.; Wang, L.; Chakraborty, N. Analysis of the flame–wall interaction in premixed turbulent combustion. *J. Fluid Mech.* **2018**, *848*, 193–218. [CrossRef]
32. Zhang, Z.; Liu, F.; An, Y.; Gao, H.; Du, W.; Gao, Y.; Lou, J. Effect of wall surface temperature on ignition and combustion characteristics of diesel fuel spray impingement. *Appl. Therm. Eng.* **2018**, *137*, 47–53. [CrossRef]
33. Tamadonfar, P.; Salomaa, V.-P.; Rintanen, A.; Karimkashi, S.; Zirwes, T.; Vuorinen, V.; Kaario, O. A numerical study on side-wall quenching of premixed laminar flames: An analysis of ammonia/hydrogen/air mixtures. *Combust. Flame* **2025**, *275*, 114100. [CrossRef]
34. Poinsot, T.; Veynante, D. Theoretical and Numerical Combustion. Available online: https://elearning.cerfacs.fr/combustion/ (accessed on 19 December 2024).
35. Ma, Z.; Henein, N.A.; Bryzik, W. A Model for Wear and Friction in Cylinder Liners and Piston Rings. *Tribol. Trans.* **2006**, *49*, 315–327. [CrossRef]
36. Willems, R.; Willems, F.; Deen, N.; Somers, B. Heat release rate shaping for optimal gross indicated efficiency in a heavy-duty RCCI engine fueled with E85 and diesel. *Fuel* **2021**, *288*, 119656. [CrossRef]
37. Leppänen, A.; Kumpula, A.; Vaara, J.; Cattarinussi, M.; Könnö, J.; Frondelius, T. Thermomechanical Fatigue Analysis of Cylinder Head. *Raken. Mek.* **2017**, *50*, 182–185. [CrossRef]
38. Nanda, S.; Jia, B.; Smallbone, A.; Roskilly, A. Fundamental Analysis of Thermal Overload in Diesel Engines: Hypothesis and Validation. *Energies* **2017**, *10*, 329. [CrossRef]
39. Wang, D.; Shi, Z.; Yang, Z.; Chen, H.; Wang, M.; Li, Y. Numerical analysis of heat transfer between a wall and diesel spray: Effect on ignition characteristics. *Fuel* **2023**, *334*, 126595. [CrossRef]
40. Kikusato, A.; Kusaka, J.; Daisho, Y. *A Numerical Study on Predicting Combustion Chamber Wall Surface Temperature Distributions in a Diesel Engine and Their Effects on Combustion, Emission and Heat Loss Characteristics by Using a 3D-CFD Code Combined with a Detailed Heat Transfer Model*; SAE International: Warrendale, PA, USA, 2015. [CrossRef]
41. Thermodynamics and Fluid Mechanics Group; Annand, W.J.D. Heat Transfer in the Cylinders of Reciprocating Internal Combustion Engines. *Proc. Inst. Mech. Eng.* **1963**, *177*, 973–996. [CrossRef]

42. Hohenberg, G.F. *Advanced Approaches for Heat Transfer Calculations*; SAE International: Warrendale, PA, USA, 1979. [CrossRef]
43. Woschni, G. *A Universally Applicable Equation for the Instantaneous Heat Transfer Coefficient in the Internal Combustion Engine*; SAE International: Warrendale, PA, USA, 1967. [CrossRef]
44. Chang, J.; Güralp, O.; Filipi, Z.; Assanis, D.; Kuo, T.-W.; Najt, P.; Rask, R. New Heat Transfer Correlation for an HCCI Engine Derived from Measurements of Instantaneous Surface Heat Flux. *SAE Trans.* **2004**, *113*, 1576–1593.
45. Eichmeier, J.U.; Reitz, R.D.; Rutland, C. A Zero-Dimensional Phenomenological Model for RCCI Combustion Using Reaction Kinetics. *SAE Int. J. Engines* **2014**, *7*, 106–119. [CrossRef]
46. Neshat, E.; Saray, R.K. Effect of different heat transfer models on HCCI engine simulation. *Energy Convers. Manag.* **2014**, *88*, 1–14. [CrossRef]
47. Mikulski, M.; Bekdemir, C.; Willems, F.P.T. Experimental validation of a combustion kinetics based multi-zone model for natural gas-diesel RCCI engines. In Proceedings of the 2016 Symposium for Combustion Control (SCC 2016), Aachen, Germany, 15–16 June 2016.
48. Christiansen, C.A. Heat Transfer in Two-Stroke Diesel Engines for Large Ship Propulsion. Ph.D. Thesis, Technical University of Denmark, Lyngby, Denmark, 2012.
49. Rakopoulos, C.D.; Mavropoulos, G.C. Experimental instantaneous heat fluxes in the cylinder head and exhaust manifold of an air-cooled diesel engine. *Energy Convers. Manag.* **2000**, *41*, 1265–1281. [CrossRef]
50. Wilhelmsson, C.; Vressner, A.; Tunestål, P.; Johansson, B.; Särner, G.; Aldén, M. *Combustion Chamber Wall Temperature Measurement and Modeling During Transient HCCI Operation*; SAE International: Warrendale, PA, USA, 2005. [CrossRef]
51. Broatch, A.; Olmeda, P.; Margot, X.; Escalona, J. New approach to study the heat transfer in internal combustion engines by 3D modelling. *Int. J. Therm. Sci.* **2019**, *138*, 405–415. [CrossRef]
52. Torregrosa, A.; Olmeda, P.; Degraeuwe, B.; Reyes, M. A concise wall temperature model for DI Diesel engines. *Appl. Therm. Eng.* **2006**, *26*, 1320–1327. [CrossRef]
53. Berni, F.; Fontanesi, S. A 3D-CFD methodology to investigate boundary layers and assess the applicability of wall functions in actual industrial problems: A focus on in-cylinder simulations. *Appl. Therm. Eng.* **2020**, *174*, 115320. [CrossRef]
54. Kim, N.; Ko, I.; Min, K. Development of a zero-dimensional turbulence model for a spark ignition engine. *Int. J. Engine Res.* **2019**, *20*, 441–451. [CrossRef]
55. Cho, S.; Song, C.; Kim, N.; Oh, S.; Han, D.; Min, K. Influence of the wall temperatures of the combustion chamber and intake ports on the charge temperature and knock characteristics in a spark-ignited engine. *Appl. Therm. Eng.* **2021**, *182*, 116000. [CrossRef]
56. Salahi, M.M.; Mahmoudzadeh Andwari, A.; Kakoee, A.; Hyvonen, J.; Gharehghani, A.; Mikulski, M.; Lendormy, É. *Novel Chemical Kinetics Mechanism for Robust Simulation of Multi-Component Fuel Blends in Engine Conditions*; SAE International: Warrendale, PA, USA, 2024. [CrossRef]
57. Zhang, H.; Cui, Y.; Liang, G.; Li, L.; Zhang, G.; Qiao, X. Fatigue life prediction analysis of high-intensity marine diesel engine cylinder head based on fast thermal fluid solid coupling method. *J. Braz. Soc. Mech. Sci. Eng.* **2021**, *43*, 327. [CrossRef]
58. Patil, M.M.; Pise, A.; Gokhale, N. *Simulation of Conjugate Heat Transfer (CHT) Between Engine Head and Cooling Medium of Diesel Engine*; SAE International: Warrendale, PA, USA, 2015. [CrossRef]
59. Wu, M.; Pei, Y.; Qin, J.; Li, X.; Zhou, J.; Zhan, Z.S.; Guo, Q.-Y.; Liu, B.; Hu, T.G. *Study on Methods of Coupling Numerical Simulation of Conjugate Heat Transfer and In-Cylinder Combustion Process in GDI Engine*; SAE International: Warrendale, PA, USA, 2017. [CrossRef]
60. Yao, T.; Pei, Y.; Zhong, B.-J.; Som, S.; Lu, T.; Luo, K.H. A compact skeletal mechanism for n-dodecane with optimized semi-global low-temperature chemistry for diesel engine simulations. *Fuel* **2017**, *191*, 339–349. [CrossRef]
61. Millo, F.; Caputo, S.; Cubito, C.; Calamiello, A.; Mercuri, D.; Rimondi, M. *Numerical Simulation of the Warm-Up of a Passenger Car Diesel Engine Equipped with an Advanced Cooling System*; SAE International: Warrendale, PA, USA, 2016. [CrossRef]
62. Institution of Mechanical Engineers (IMechE). *Vehicle Thermal Management Systems Conference and Exhibition (VTMS10)*; Woodhead Publishing: Cambridge, UK, 2011.
63. Graziano, E.; Bruno, L.; Corrado, P.; Pierson, S.; Virelli, G. *Set-Up and Validation of an Integrated Engine Thermal Model in GT-SUITE for Heat Rejection Prediction*; SAE International: Warrendale, PA, USA, 2019. [CrossRef]
64. Jay, D. CR development in the last decade in Wärtsilä. In Proceedings of the 28th CIMAC world congress, Helsinky, Finland, 6–10 June 2016; pp. 6–10.
65. *ISO 8217:2024*; Petroleum Products—Fuels (Class F)—Specifications of Marine Fuels. International Organization for Standardization (ISO): Geneva, Switzerland, 2017.
66. Åstrand, U.; Aatola, H.; Myllykoski, J.M. Wärtsilä 31—World's Most Efficient Four Stroke Engine. In Proceedings of the 28th CIMAC Congress, Helsinki, Finland, 6–10 June 2016.
67. Vasudev, A.; Kakoee, A.; Axelsson, M.; Almani, H.M.; Hyvönen, J.; Mikulski, M. Advancing autonomy of chemical kinetics based multizone models for reactivity controlled compression ignition engines. *Energy Convers. Manag.* **2024**, *312*, 118562. [CrossRef]
68. GT-Suite. *Engine Performance Application Manual*; Gamma Technologies: Westmont, IL, USA, 2023.
69. Heywood, J.B. *Internal Combustion Engine Fundamentals*; McGraw Hill: New York, NY, USA, 1988.

70. Mikulski, M.; Ramesh, S.; Bekdemir, C. Reactivity Controlled Compression Ignition for clean and efficient ship propulsion. *Energy* **2019**, *182*, 1173–1192. [CrossRef]
71. Benajes, J.; García, A.; Pastor, J.M.; Monsalve-Serrano, J. Effects of piston bowl geometry on Reactivity Controlled Compression Ignition heat transfer and combustion losses at different engine loads. *Energy* **2016**, *98*, 64–77. [CrossRef]
72. Gu, C.; Wang, R.; Tian, T. Modeling the Fatigue Wear of the Cylinder Liner in Internal Combustion Engines during the Break-In Period and Its Impact on Piston Ring Lubrication. *Lubricants* **2019**, *7*, 89. [CrossRef]
73. Rahmani, R.; Rahnejat, H.; Fitzsimons, B.; Dowson, D. The effect of cylinder liner operating temperature on frictional loss and engine emissions in piston ring conjunction. *Appl. Energy* **2017**, *191*, 568–581. [CrossRef]
74. Apaydin, S.; Doner, N. Effects of piston cooling gallery geometry on temperature and flow in a heavy-duty diesel engine. *Therm. Sci. Eng. Prog.* **2024**, *51*, 102644. [CrossRef]
75. Margot, X.; Quintero, P.; Gomez-Soriano, J.; Escalona, J. Implementation of 1D–3D integrated model for thermal prediction in internal combustion engines. *Appl. Therm. Eng.* **2021**, *194*, 117034. [CrossRef]
76. Wei, Z.; Goehring, T.; Mioduszewski, M.; Luo, L.; Kotrba, A.; Rybarz, M.; Ellinghaus, K.; Pieszkalla, M. Failure mechanisms and modes analysis of vehicle exhaust components and systems. In *Handbook of Materials Failure Analysis with Case Studies from the Aerospace and Automotive Industries*; Elsevier: Amsterdam, The Netherlands, 2016; pp. 393–432. [CrossRef]
77. Singh, A.P.; Kumar, V.; Agarwal, A.K. Evaluation of comparative engine combustion, performance and emission characteristics of low temperature combustion (PCCI and RCCI) modes. *Appl. Energy* **2020**, *278*, 115644. [CrossRef]
78. Johnston, T.; Zeman, J.; Dempsey, A. Mixing-controlled compression ignition of ethanol using exhaust rebreathe at a low-load operating condition—Single cylinder experiments in a heavy-duty diesel engine. *Int. J. Engine Res.* **2024**, *26*, 741–764. [CrossRef]
79. Vasudev, A.; Soleimani, A.; Hyvönen, J.; Mikulski, M. Feasible route towards decarbonising marine transport with flexible, Hydrogen—Enriched, Reactivity Controlled Compression Ignition mid-speed engines. *Int. J. Hydrogen Energy* **2025**, *142*, 1196–1210. [CrossRef]
80. Huang, Z.; Zhu, T.; Wang, L.; Wang, L.; Ali, A.S.; Nassef, M.G.A.; Wang, T.; Ahmed, R.H. Experimental Analysis of Ammonia-Hydrogen Energy Ratio and Valve Overlap Angle on the Combustion and Emissions Characteristics in Dual-Fuel Internal Combustion Engines. *SSRN* **2025**. [CrossRef]
81. Rao, X.; Sheng, C.; Guo, Z.; Zhang, X.; Yin, H.; Xu, C.; Yuan, C. Effects of textured cylinder liner piston ring on performances of diesel engine under hot engine tests. *Renew. Sustain. Energy Rev.* **2021**, *146*, 111193. [CrossRef]
82. Hunicz, J.; Yang, L.; Rybak, A.; Ji, S.; Gęca, M.S.; Mikulski, M. Comparison of diesel and hydrotreated vegetable oil as the high-reactivity fuel in reactivity-controlled compression ignition. *Energy Convers. Manag.* **2025**, *323*, 119264. [CrossRef]
83. CASEMATE–Computationally Aided Systems Engineering for Marine Advanced Technology for the Environment. Available online: https://www.uwasa.fi/fi/tutkimus/hankkeet/casemate-computationally-aided-systems-engineering-marine-advanced-technology (accessed on 14 October 2022).
84. Flexible Solutions for Maritime Transport and Off-Road Machinery. Available online: https://cleanpropulsion.org/ (accessed on 14 October 2022).